

---

# On the Completeness of Invariant Geometric Deep Learning Models

---

Zian Li<sup>1,2</sup> Xiyuan Wang<sup>1,2</sup> Shijia Kang<sup>1</sup> Muhan Zhang<sup>1</sup>

## Abstract

Invariant models, one important class of geometric deep learning models, are capable of generating meaningful geometric representations by leveraging informative geometric features. These models are characterized by their simplicity, good experimental results and computational efficiency. However, their theoretical expressive power still remains unclear, restricting a deeper understanding of the potential of such models. In this work, we concentrate on characterizing the theoretical expressiveness of invariant models. We first rigorously bound the expressiveness of the most classical invariant model, Vanilla DisGNN (message passing neural networks incorporating distance), restricting its unidentifiable cases to be only those highly symmetric geometric graphs. To break these corner cases' symmetry, we introduce a simple yet E(3)-complete invariant design by nesting Vanilla DisGNN, named GeoNGNN. Leveraging GeoNGNN as a theoretical tool, we for the first time prove the E(3)-completeness of three well-established geometric models: DimeNet, GemNet and SphereNet. Our results fill the gap in the theoretical power of invariant models, contributing to a rigorous and comprehensive understanding of their capabilities. Experimentally, GeoNGNN exhibits good inductive bias in capturing local environments, and achieves competitive results w.r.t. complicated models relying on high-order invariant/equivariant representations while exhibiting significantly faster computational speed.

## 1. Introduction

Learning geometric structural information from 3D point sets constitutes a fundamental requirement for various real-world applications, including molecular property pre-

---

<sup>\*</sup>Equal contribution <sup>1</sup>Institute for Artificial Intelligence, Peking University <sup>2</sup>School of Intelligence Science and Technology, Peking University. Correspondence to: Muhan Zhang <muhan@pku.edu.cn>.

Preprint. Under review.

diction, physical simulation, and point cloud classification/segmentation (Schmitz et al., 2019; Sanchez-Gonzalez et al., 2020; Jumper et al., 2021; Guo et al., 2020).

In the context of designing geometric models for 3D point sets, a pivotal consideration involves ensuring that the model respects both permutation symmetry and Euclidean symmetry (i.e., symmetry of SE(3) or E(3) group). This requirement necessitates the incorporation of appropriate inductive biases into the architecture, ensuring that the model's output remains invariant or equivariant to point reordering and 3D rigid motion (and potentially reflection).

However, these restrictions on *symmetry* can impose limitations on the ability of models to approximate a broad range of symmetric functions. For example, Message Passing Neural Networks (MPNNs) (Gilmer et al., 2017), a wide class of Graph Neural Networks (GNNs), learn permutation symmetric functions w.r.t. node reordering. However, it has been shown that such functions are not universal (Xu et al., 2018; Morris et al., 2019), leading to the development of more expressive GNN frameworks (Maron et al., 2018; Morris et al., 2019; Zhang et al., 2023). Similar challenges arise in the geometric setting, where models must additionally respect the Euclidean symmetry, and achieving universality becomes a non-trivial task as well.

Recent studies (Pozdnyakov & Ceriotti, 2022; Li et al., 2023b) have demonstrated that a simple invariant geometric model, SchNet (Schütt et al., 2018), which incorporates Euclidean distance into MPNNs, is not E(3)-complete, failing to distinguish pairs of non-E(3)-isomorphic geometric graphs. In order to design more powerful invariant geometric models, recent works (Gasteiger et al., 2019; 2022; Schütt et al., 2018) incorporate higher-order geometric information or leverage spherical coordinates, making their models able to identify some corner symmetric cases. However, these works do not provide a theoretical completeness guarantee; thus, whether these models have the potential to achieve completeness is still to be studied.

In this work, we for the first time analyze the completeness, i.e., ability to distinguish any non-isomorphic geometric graphs, across a wide range of invariant geometric models. Completeness is important since it is equivalent to the ability of models to universally approximate corresponding functions (Hordan et al., 2023).

We begin by revisiting Vanilla DisGNN, the simplest conceptual invariant model augmenting MPNNs with distance as an edge feature (SchNet is a concrete implementation of it), with a specific emphasis on addressing the question: when is Vanilla DisGNN powerful enough? We demonstrate that Vanilla DisGNN can effectively acquire global geometric information and achieve lossless encoding for geometric graphs under the condition that there exists *two distinct global anchors*. Consequently, we establish that Vanilla DisGNN is a *nearly-E(3)-complete* model by restricting all its unidentifiable cases into a small subspace that only contains well-defined highly-symmetric geometric graphs.

To break these unidentifiable cases’ symmetry and enhance Vanilla DisGNN’s expressiveness, we introduce GeoNGNN, the geometric counterpart of NGNN (Zhang & Li, 2021) (one of the simplest subgraph GNNs), which runs Vanilla DisGNN in a nested way. We theoretically establish that GeoNGNN is an E(3)-complete geometric model, capable of identifying all geometric graphs. We also propose an *SE(3)-complete* variant of GeoNGNN, named GeoNGNN-C, which is capable of bracing chirality and learning different representations for pairs of enantiomers.

Importantly, GeoNGNN serves as a tool for proving other invariant models’ expressiveness: By reducing three well-established invariant geometric models, DimeNet (Gasteiger et al., 2019), SphereNet (Liu et al., 2021) and GemNet (Gasteiger et al., 2021), onto GeoNGNN, we for the first time demonstrate that these models are all *capable of achieving E(3)-completeness* under certain conditions.

Our theoretical findings narrow the gap between experimental advancements and theoretical characterizations of invariant geometric models during these years, contributing to a rigorous and comprehensive understanding of their capabilities. Most importantly, the findings suggest that the geometric graph isomorphism problem is *fundamentally easier* than the traditional graph isomorphism problem, indicating that achieving geometric completeness is not as intractable as that in the traditional setting.

Despite not focusing on model enhancement, we still thoroughly evaluate GeoNGNN on diverse datasets. GeoNGNN achieves competitive performance to models that incorporate complicated high-order invariant or equivariant representations, and demonstrates significantly faster speed when applied to large molecules (with up to 300 atoms).

## 2. Preliminary

### 2.1. Notations and Definitions

**Notation.** We represent a 3D geometric graph with  $n$  nodes as its minimal representation, i.e., point clouds:  $G = (X, P)$ , where  $X \in \mathbb{R}^{n \times d}$  and  $P \in \mathbb{R}^{n \times 3}$  repre-

sents the initial node features and 3D Cartesian coordinates of the  $n$  nodes respectively. Euclidean distance between node  $i$  and  $j$  is represented by  $d_{ij}$ .

**Definition 2.1. (E(3)-isomorphic)** Two geometric graphs  $G^{(1)}, G^{(2)}$  are E(3)-isomorphic if they have the same node number  $n$ , and there exist permutation matrix  $\mathcal{P} \in \{0, 1\}^{n \times n}$ , rotation/reflection matrix  $\mathcal{R} \in O(3)$  and translation matrix  $\mathcal{T} \in \mathbb{R}^3$  such that  $\mathcal{P}X^{(1)} = X^{(2)}$  and  $(\mathcal{P}P^{(1)})\mathcal{R}^T + \mathcal{T} = P^{(2)}$  (+ considers broadcast).

**Definition 2.2. (Identifiability and E(3)-completeness)** Let  $f$  be a permutation- and E(3)-invariant algorithm that takes geometric graphs  $G$  with arbitrary size as input, and outputs scalars  $s \in \mathbb{R}^k$ . We say  $f$  can *identify*  $G$ , if for an arbitrary geometric graph  $G'$  that is not E(3)-isomorphic to  $G$ ,  $f(G) \neq f(G')$ . We say  $f$  is *E(3)-complete*, if given two arbitrary geometric graphs  $G^{(1)}$  and  $G^{(2)}$ ,  $f(G^{(1)}) = f(G^{(2)}) \iff G^{(1)}$  and  $G^{(2)}$  are E(3)-isomorphic.

It is easy to see that identifiability and E(3)-completeness are related:  $f$  can identify all geometric graphs  $\iff f$  is E(3)-complete. However, identifiability provides a more fine-grained characterization of E(3)-incomplete models. In the analysis of Vanilla DisGNN’s E(3)-incompleteness, we concentrate on the commonality of its unidentifiable graphs.

Depending on the context, the terms *expressiveness* or *power* are used to describe the capability of algorithms to distinguish between non-isomorphic topological graphs or non-E(3)-isomorphic geometric graphs.

During the theoretical analysis, we are particularly concerned about powerful encoders that encode input representations without significant information loss. We provide a formal definition of an important concept *derive* below:

**Definition 2.3. (Derive)** Given input representations  $I \in \mathcal{I}$ , let  $f : \mathcal{I} \rightarrow \mathcal{O}_1$  and  $g : \mathcal{I} \rightarrow \mathcal{O}_2$  be two property encoders defined on  $\mathcal{I}$ . If there exists a function  $h : \mathcal{O}_1 \rightarrow \mathcal{O}_2$  such that for all  $I \in \mathcal{I}$ ,  $h(f(I)) = g(I)$ , we say that  $f$  can derive  $g$ . With a slight abuse of notation, we say that  $f(I)$  can derive  $g(I)$ , denoted as  $f(I) \rightarrow g(I)$ .

For example, consider the space  $\mathcal{I}$  comprising all geometric graphs. Let  $f$  denote an encoder that computes  $f(I) = (\sum_{i=0}^{n-1} P_i, n)$ , which represents the sum of the nodes’ coordinates and the number of nodes, while  $g$  being an encoder calculating the geometric center of  $I$ , it follows that  $f(I) \rightarrow g(I)$ . Note that derivation exhibits transitivity: if  $f_1 \rightarrow f_2$  and  $f_2 \rightarrow f_3$ , it follows that  $f_1 \rightarrow f_3$ .

Different from identifiability, which describes a given algorithm’s ability to distinguish geometric graphs, “derive” is a broader concept describing the relation of two intermediate properties, i.e., whether a property  $f(I)$  contains all the information needed to calculate  $g(I)$ . However, they are also related: consider  $\mathcal{I}$  being the geometric graph space

and  $f$  satisfying permutation- and E(3)-invariance, then:  $f(I) \rightarrow I$  up to permutation and E(3)-transformation  $\iff f$  is E(3)-complete  $\iff f$  can identify all  $I \in \mathcal{I}$ . The proof is presented in Appendix F.1.

## 2.2. Vanilla DisGNN

To leverage the rich geometric information present in geometric graphs, an early and straightforward approach is to use the pair-wise Euclidean distance  $d_{ij}$  as a basic geometric feature. This approach applies MPNNs on the *distance graph* with a weighted edge  $e_{ij}$  between any pairs of nodes  $i, j$  if  $d_{ij} \leq r$  ( $r$  is some predefined cutoff). SchNet (Schütt et al., 2018) is a representative of such works.

To be specific, Vanilla DisGNN models first embed atoms based on their initial feature  $X$ , such as atomic numbers, obtaining  $h_i^{(0)}$  for node  $i$ . They then perform message passing according to the following equation iteratively:

$$h_i^{(t+1)} = f_{\text{update}}^{(t)} \left( h_i^{(t)}, f_{\text{aggr}}^{(t)} \left( \{ \{ h_j^{(t)}, d_{ij} \} \mid j \in N(i) \} \right) \right), \quad (1)$$

where  $h_i^{(t)}$  represents the node embedding for node  $i$  at time step  $t$ ,  $N(i)$  denotes the neighbor set of node  $i$ . The global graph embedding is then obtained by aggregating the representations of all nodes using a permutation-invariant function  $f_{\text{out}}(\{ \{ h_i^T \mid i \in [n] \} \})$ , where  $T$  is the total number of layers and  $n$  is the total number of nodes.

If the hidden dimension is sufficiently large and the intermediate functions used are powerful enough (Hornik et al., 1989; Zaheer et al., 2017; Xu et al., 2018), the intermediate functions can be learned to be nearly injective, resulting in lossless transformation. We regard this as a default assumption throughout the theoretical analysis. This assumption is reasonable since the expressive power of models/algorithms is fundamentally limited by their framework design (Xu et al., 2018; Maron et al., 2018; Morris et al., 2019), rather than layer width. Furthermore, in our theoretical analysis, we assume that  $N(i)$  is  $[n]$  by default, i.e., global message passing, which grants models the maximum expressiveness (we aim to study their maximal potential). Note that both assumptions align with existing works in the literature (Li et al., 2023b; Pozdnyakov & Ceriotti, 2022; Delle Rose et al., 2023; Dym & Maron, 2020; Hordan et al., 2023).

## 2.3. Nested Graph Neural Network

Nested GNN (NGNN) (Zhang & Li, 2021) is a subgraph GNN proposed initially in traditional graph representation learning field. The algorithm performs a two-level GNN on a given graph. The first level, known as the inner GNN, runs concurrently on each node’s  $k$ -hop ego subgraph with the center node optionally marked (gives it a distinct feature), summarizing the local subgraph information as the nodes’ initial embedding in the original graph. Then, the second

level, referred to as the outer GNN, runs on the original graph to obtain the final node and graph representations.

NGNN encodes nodes’ local subgraph information as their initial embeddings, rather than subtree information, which makes it strictly more powerful than MPNNs such as GIN (Xu et al., 2018). However, Zhang et al. (2023) pointed out that NGNN is a relatively weaker subgraph GNN in learning topological graph structures than Qian et al. (2022); Zhao et al. (2021); Bevilacqua et al. (2021); Frasca et al. (2022), since it does not contain cross-subgraph operations which pass messages across different subgraphs. In our work, we present a surprising result, showing that in geometric settings, NGNN is indeed sufficient.

## 3. How powerful is Vanilla DisGNN?

In Pozdnyakov & Ceriotti (2022); Li et al. (2023b), researchers have carefully constructed pairs of symmetric geometric graphs that Vanilla DisGNN cannot distinguish to illustrate its E(3)-incompleteness. However, rather than relying on hand-crafted finite pairs of counterexamples and intuitive illustration, a more significant question arises: *what properties do all the geometric graphs that Vanilla DisGNN cannot identify share in common?* Only after theoretically characterizing these corner cases can we describe and bound the expressiveness of Vanilla DisGNN in a finer way, and then design more powerful geometric models accordingly by “solving” these corner cases.

In this section, we begin by demonstrating the inherent ability of Vanilla DisGNN to locate “anchors”, which enables the model to capture global geometric information. Subsequently, we present an essential theorem that establishes how Vanilla DisGNN can achieve lossless encoding of a geometric graph with the presence of two distinct anchors. With these findings, we finally restrict the unidentifiable cases of Vanilla DisGNN solely to those highly symmetric graphs naturally lacking multiple anchors.

### 3.1. Ability to Locate Global Anchors

Before proceeding, we provide a formal definition of *anchors*. Given a geometric graph  $G$ , we define an anchor function as  $A(G) : \mathbb{R}^{n \times d} \times \mathbb{R}^{n \times 3} \rightarrow \mathbb{R}^3$ , which calculates an anchor coordinate in a *permutation invariant* and *E(3)-equivariant* manner. If the context is clear, we omit  $(G)$  and use  $A$  to represent the anchor’s 3D coordinates and use  $d_{i,A}$  to denote the distance between node  $i$  and the anchor.

We then introduce a simple but comprehensive set of anchors, referred to as *global anchors*. Each global anchor is characterized by a “mass function”  $m : \mathbb{R}^d \rightarrow \mathbb{R}$ , which maps the features of a node to a generalized node mass. Subsequently, we define the global anchor as follows:

**Definition 3.1. (Global Anchor, GA)** Given a geometric

graph  $G = (X, P)$  and a mass function  $m : \mathbb{R}^d \rightarrow \mathbb{R}$  that satisfies  $\sum_{i \in [n]} m(X_i) \neq 0$ , the corresponding global anchor is defined as:  $A^m(G) = \frac{\sum_{i \in [n]} m(X_i) P_i}{\sum_{i \in [n]} m(X_i)}$ .

Global anchor encompasses a broad range of anchors. Representative global anchors include: 1) Geometric center, where  $m$  maps all  $X_i$  to 1. 2) Barycenter (in chemical/physical systems), where  $m$  maps  $X_i$  to the physical mass of node  $i$ . 3)  $X^*$ -type geometric center, where  $m$  maps  $X_i = X^*$  to 1 and  $X_i \neq X^*$  to 0.

We denote the set of all global anchors of graph  $G$  as  $\mathbf{A}(G) = \{A^m(G) \mid m : \mathbb{R}^d \rightarrow \mathbb{R}, \sum_{i \in [n]} m(X_i) \neq 0\}$ . Note that since we iterate all  $m$  functions,  $\mathbf{A}(G)$  is dependent only on the individualization of node features but invariant to feature values. An illustration of global anchor sets is shown in Figure 1.

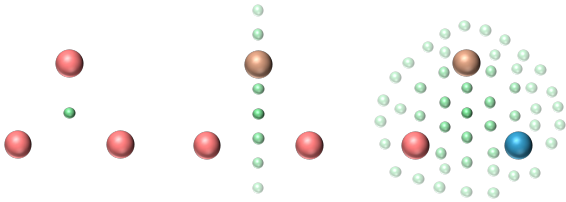


Figure 1. Global anchor set. The three colored balls represent a triangle-shaped geometric graph, where different colors indicate different node features. The small green balls indicate global anchors with different mass functions. From left to right, geometric graphs with more global anchors exhibit worse symmetry.

Intuitively, by learning the Euclidean distance between nodes and anchors, the model can acquire significant global geometric information about a given graph, enabling itself to produce more meaningful geometric representations. Now, we present a preliminary conclusion regarding such geometric learning capability of Vanilla DisGNN:

**Proposition 3.2.** (*Locate Global Anchors*) Given a geometric graph  $G$ , denote node  $i$ 's representation produced by 2-round Vanilla DisGNN as  $h_i^{(2)}$ , then we have:

- (Node-GA distance) Given an arbitrary mass function  $m$ ,  $h_i^{(2)}$  can derive  $d_{i, A^m}$ .
- (GA-GA distance) Given two arbitrary mass functions  $m_1$  and  $m_2$ ,  $\{h_i^{(2)} \mid i \in [n]\}$  can derive  $d_{A^{m_1}, A^{m_2}}$ .
- (Counting GA)  $\{h_i^{(2)} \mid i \in [n]\}$  can derive  $\mathbb{1}_{|\mathbf{A}(G)|=1}$ .

Proposition 3.2 can be regarded as a generalization of the Barycenter Lemma presented in Delle Rose et al. (2023), which only shows the ability of Vanilla DisGNN to learn distance from nodes to geometric center. It establishes that Vanilla DisGNN possesses the ability to automatically incorporate the *triangle* information, formed by the node and any two global anchors, into the node features. In the subsequent

subsection, we will demonstrate the theoretical utilization of such ability to fully encode a given geometric graph.

### 3.2. Two Anchors are Enough for Lossless Encoding

We first introduce the concept of Anchor Positional Encoding (APE) and subsequently establish an important theorem relating to APE which characterizes the geometric encoding capability of Vanilla DisGNN.

**Definition 3.3.** (Anchor Positional Encoding, APE) Given a geometric graph  $G = (X, P)$ , assume there are two *distinct* anchors on it, represented as  $A_1, A_2 \in \mathbb{R}^3$ . APE enhances node  $i$ 's feature  $X_i$  to  $X'_i$  through an injective function  $X'_i = f_{\text{APE}}(X_i, d_{i, A_1}, d_{i, A_2}, d_{A_1, A_2})$ . We denote the application of  $f_{\text{APE}}$  on  $X$  row-wisely as  $X' = f_{\text{APE}}^*(X_i, d_{i, A_1}, d_{i, A_2}, d_{A_1, A_2})$ .

By definition, APE is performed relative to two distinct anchors (not limited to global anchors), enhancing node features with the *triangle* information w.r.t. the node and the two anchors. APE can enhance the encoding power of Vanilla DisGNN, as stated in the following theorem:

**Theorem 3.4.** (*Vanilla DisGNNs' encoding power with APE*) Given a geometric graph  $G = (X, P)$ , assume there are two *distinct* anchors on it, represented as  $A_1, A_2 \in \mathbb{R}^3$ . We first enhance the geometric graph to  $G' = (f_{\text{APE}}^*(X), P)$  through APE, then we have:  $G'$  can be derived from a two-layer Vanilla DisGNN's output on  $G'$  up to permutation and  $E(3)$ -transformation.

Theorem 3.4 essentially demonstrates that Vanilla DisGNN with APE can attain  $E(3)$ -completeness on the *subspace*  $\mathcal{G}'$  of the geometric graph space  $\mathcal{G}$ , where all  $G \in \mathcal{G}'$  satisfy the assumption that there exist two distinct anchors on  $G$ . In the following text, we use Theorem 3.4 as a base theorem to analyze Vanilla DisGNN's inherent expressiveness and motivate new powerful designs.

### 3.3. Restricting Unidentifiable Cases into a Small Space

By combining Proposition 3.2 and Definition 3.3, we can conclude that Vanilla DisGNN can *automatically* perform APE w.r.t. two *global anchors*. And as indicated by Theorem 3.4, with such ability, Vanilla DisGNN can losslessly encode all geometric graphs with more than two global anchors, leading to the following necessary condition:

**Theorem 3.5.** (*Necessary condition for unidentifiable cases*) Given a geometric graph  $G$ , Vanilla DisGNN cannot identify  $G$  only if  $|\mathbf{A}(G)| = 1$ .

Indeed, all geometric graphs whose global anchor set degenerates, namely  $|\mathbf{A}(G)| = 1$ , are highly symmetric, which we define as **GA-symmetric**<sup>1</sup>. See Figure 1 for an illus-

<sup>1</sup>The determination of whether a graph is GA-symmetric does

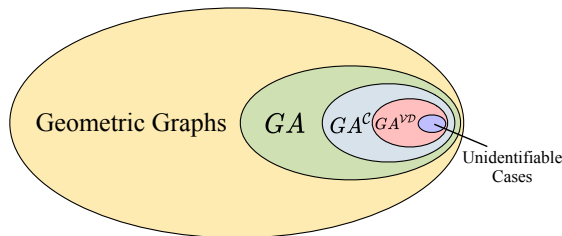


Figure 2. Illustration of the unidentifiable cases of Vanilla DisGNN. Parts with  $GA^S$  contains all the  $GA^S$ -symmetric graphs, where  $S$  can be empty,  $C$  or  $VD$ . All the parts strictly contain their sub-parts (proper subset relation), which is detailed in Appendix A. The unidentifiable graphs by Vanilla DisGNN are constrained to be highly symmetric, i.e.,  $GA^{VD}$ -symmetric, geometric graphs.

tration of how  $|A(G)|$  reflects the degree of symmetry of a given geometric graph. Therefore, Theorem 3.5 gives the commonality that all unidentifiable cases of Vanilla DisGNN possess, essentially limiting the space of unidentifiable cases to a significantly restricted region that contains only those highly symmetric geometric graphs, as shown by the purple part in Figure 2. Note that the intuitive unidentifiable constructions by Pozdnyakov & Ceriotti (2022); Li et al. (2023b) all validate our conclusion, but Theorem 3.5 for the first time gives a formal definition of “symmetry”.

From Theorem 3.5, one can readily determine which geometric graphs can be identified by Vanilla DisGNN. For example, nearly all molecules such as aspirin and ethanol are not  $GA$ -symmetric, thus can be identified by Vanilla DisGNN. As a consequence, Vanilla DisGNN can produce a unique geometric representation/fingerprint for them safely.

However, up to this point, one may find that the restriction of unidentifiable cases is relatively loose: All raw point clouds lacking initial node features (i.e., with identical node features) are naturally  $GA$ -symmetric due to the absence of node individualization, and consequently, we are still unable to determine if Vanilla DisGNN can identify these cases based on the necessary condition 3.5. To address this limitation, we introduce two **higher-level** symmetries, namely  $GA^C$ - and  $GA^{VD}$ -symmetry, which further limit the scope of unidentifiable cases to a significantly smaller subset of  $GA$ -symmetric graphs, and show that most point clouds without node features are still identifiable by Vanilla DisGNN. This refinement allows us to characterize the expressive power of Vanilla DisGNN much more precisely. An informative visual representation of the relation graph is in Figure 2. To further understand how rare the cases Vanilla DisGNN cannot identify are, we investigate the proportion of  $GA^{VD}$ -symmetric graphs in real-world datasets, including QM9 and ModelNet. Even with the largest tolerance error, the proportion of unidentifiable cases amounts to **less**

not require iterating through all  $m$  functions. We provide a simplified, finite-step algorithm in Proposition A.3 in Appendix A.1.

than 0.1% of the whole set of examined geometric graphs. For these extended analysis of Vanilla DisGNN, we direct the readers to Appendix A.

## 4. On the Completeness of Invariant Models

In this section, we demonstrate and prove the  $E(3)$ -completeness of a wide range of invariant models under certain conditions. These models can effectively “solve” all the highly-symmetric, i.e.,  $GA$ -symmetric, geometric graphs that Vanilla DisGNN may not identify. We first introduce a new simple invariant model design, which can break such symmetry and identify these graphs. Consequently, we show how this new design serves as a theoretical tool for proving a series of invariant models’ expressiveness.

### 4.1. Breaking Symmetry Utilizing Local Anchors

Based on the analysis in Section 3.2 and 3.3, it is evident that for  $GA$ -symmetric graphs, if we are able to **determine and specify an additional anchor** beyond the unique global anchor, Vanilla DisGNN becomes able to identify all of them. However, for certain extremely symmetric graphs such as a sphere, all possible anchors naturally degenerate into the geometric center. Consequently, no additional anchors beyond the global anchor can be obtained.

We now demonstrate that the geometric counterpart of NGNN (Zhang & Li, 2021), named GeoNGNN, can precisely break such symmetry utilizing *local anchors*. We first formally give the definition of GeoNGNN:

**Definition 4.1.** (GeoNGNN) GeoNGNN is the geometric version of NGNN (Zhang & Li, 2021), which takes geometric graphs  $G = (X, P)$  as input, and:

- Both the inner and outer GNN adopt Vanilla DisGNN, with each consisting of  $N_{in}$  and  $N_{out}$  layers, respectively.
- The node marking policy is employed.
- The ego subgraph of each node contains all nodes within a Euclidean distance cutoff  $r_{sub}$ .

GeoNGNN adopts the same framework of NGNN, except that it is tailored for geometric settings: the subgraph cutoff is defined on Euclidean distance instead of “hop”, while the base model is the simplest invariant geometric model, Vanilla DisGNN. Leveraging Theorem 3.4, we give the conditions for GeoNGNN to achieve  $E(3)$ -completeness:

**Theorem 4.2.** ( $E(3)$ -Completeness of GeoNGNN) When the following conditions are met, GeoNGNN is  $E(3)$ -complete:

- $N_{in} \geq 5$  and  $N_{out} \geq 0$  (0 means that outer GNN only performs an injective pooling).
- $r_{sub} = +\infty$ .
- Inner GNN performs global message passing.

The key idea behind Theorem 4.2 is intuitive: the addition-

ally marked node  $i$  in its subgraph acts as an extra anchor, i.e., the *local anchor*. Together, this additional anchor and the geometric center (a global anchor) serve as two distinct anchors, therefore satisfying the assumptions specified in Theorem 3.4, and ultimately leading to the completeness of Vanilla DisGNN. Despite that node  $i$  can still coincide with the geometric center, GeoNGNN applies Vanilla DisGNN to every node in parallel, ensuring that there always exists some node  $i$  which is distinct from the geometric center.

Unlike global anchors which are calculated in a permutation-invariant manner, local anchors do not maintain invariance but break it. However, since GeoNGNN pools all the local anchors, the overall permutation invariance is preserved.

#### 4.2. Completeness of Well-Established Invariant Models

Now, based on the completeness of GeoNGNN, we move on to establish that several well-known invariant models, DimeNet (Gasteiger et al., 2019), GemNet (Gasteiger et al., 2021) and SphereNet (Liu et al., 2021) can all achieve E(3)-completeness under certain conditions, by *reducing them onto* GeoNGNN (see Appendix F.7 for the description of these models and the formal proof).

**Theorem 4.3.** (*E(3)-Completeness of DimeNet, SphereNet, GemNet*) When the following conditions are met, DimeNet, SphereNet<sup>2</sup> and GemNet are E(3)-complete.

- They initialize and update all edge representations.
- They perform global message passing<sup>3</sup>.
- The message passing layer number is larger than some constant  $C$ .

A key insight behind Theorem 4.3 is that, all these models track edge representations ( $h_{ij}^{edge}$  for edge  $(i, j)$ ), which can be mathematically aligned with the node-subgraph representations tracked in GeoNGNN ( $h_{ij}^{subg}$  for node  $i$  in subgraph  $j$ ). Consequently, these three models can be mathematically reduced to GeoNGNN.

Theorem 4.3 for the first time highlights that the relatively simple invariant model, DimeNet, is already E(3)-complete. Consequently, subsequent efforts like GemNet, which incorporates higher-order geometry, could be unnecessary in terms of boosting theoretical expressiveness. However, we note that even though a wide range of invariant models are equally expressive, they may possess differing inductive biases, leading to distinct levels of generalization power and experimental performance, as validated in Li et al. (2023b).

<sup>2</sup>Here in SphereNet we do not consider the relative azimuthal angle  $\varphi$ , since SphereNet with  $\varphi$  is not E(3)-invariant, while E(3)-completeness is defined on E(3)-invariant models. Note that the exclusion of  $\varphi$  only results in weaker expressiveness.

<sup>3</sup>In DimeNet and GemNet, nodes  $i$  or  $j$  are excluded when aggregating neighbors for edge  $ij$ . The condition requires the inclusion of these end nodes.

## 5. Related Work

Geometric models leverage the rich 3D geometric information contained in geometric graphs (Han et al., 2022), and aim to learn meaningful geometric representations while respecting permutation and Euclidean symmetry. Earlier work by Schütt et al. (2018) integrated 3D Euclidean distance into the MPNN framework (Gilmer et al., 2017), making the model invariant to permutations and E(3) transformations. Nevertheless, this model exhibits a restricted capacity to distinguish non-E(3)-isomorphic geometric graphs even on fully-connected graphs as substantiated by Li et al. (2023b); Pozdnyakov & Ceriotti (2022). Subsequent invariant models (Gasteiger et al., 2019; 2020; 2021; 2022; Liu et al., 2021) have endeavored to enhance expressiveness by incorporating invariant high-order geometric features or adopting local spherical representations. Several works also adopt vector representations to enhance model’s theoretical and experimental performance (Satorras et al., 2021; Schütt et al., 2021; Thölke & De Fabritiis, 2021; Deng et al., 2021). However, all these methods suffer from a lack of theoretical guarantee of 3D completeness.

Another line of equivariant methods leverage high-order SO(3) irreducible representations (Thomas et al., 2018; Fuchs et al., 2020; Batatia et al., 2022; Batzner et al., 2022; Brandstetter et al., 2021; Musaelian et al., 2023), which come with the theoretical guarantee of universality (Dym & Maron, 2020). However, these models necessitate infinite-order spherical tensors for approximating high-order polynomials, which is intractable due to the need for expensive tensor products (in practice, the order is less than 3). Other methods project the coordinates or vector features onto local or global equivariant frames to ensure models’ Euclidean symmetry (Wang & Zhang, 2022; Duval et al., 2023; Puny et al., 2021). These methods, however, are based on the assumption of non-degenerate frames, thereby making them incapable of processing almost all symmetric geometric graphs, which are exactly the corner cases we aim to capture. Recently, (Li et al., 2023b) proposed a theoretically complete invariant framework by generalizing  $k$ -(F)WL methods (Weisfeiler & Leman, 1968; Cai et al., 1992) for graph isomorphism test to the geometric setting. Nonetheless, the framework faces difficulty in scaling to large geometric graphs. Moreover, Li et al. (2023b) cannot be extended to SE(3)-completeness cases, which are quite important for capturing the chirality of molecules or general 3D geometric graphs.

## 6. Experiments

In this section, we aim to answer the following questions:

- **Q1.** Can GeoNGNN effectively distinguish counterexamples pairs of geometric graphs that cannot be distinguished

by Vanilla DisGNN?<sup>4</sup>

- **Q2.** Can the practical GeoNGNN<sup>5</sup>, which simply enhances Vanilla DisGNN with local subgraphs, achieve competitive performance compared to complex models adopting high-order invariant/equivariant representations, while exhibiting faster inference due to the simple design?
- **Q3.** How do subgraph sizes, which serve as a trade-off between theoretical completeness and experimental tractability, affect the performance of GeoNGNN?

**Variants of GeoNGNN.** Beyond beforehand questions, we also introduce and evaluate two important variants of GeoNGNN in Appendix D, E. The first one is GeoNGNN-C, an **SE(3)-complete** variant of GeoNGNN, designed by simply replacing the undirected distances in GeoNGNN with directed ones. GeoNGNN-C embraces *chirality* and is capable of learning meaningful chirality-relevant representations for achieving good performances in downstream tasks. The second one is GeoNGNN with **sampling policies**, which improves the efficiency of GeoNGNN by avoiding running Vanilla DisGNN on all local anchors’ subgraphs. Nonetheless, this design yields primarily negative results, underscoring the importance of leveraging all local anchors for both theoretical soundness and faithfulness for practical physical and chemical systems.

**Models to compare with.** We compare GeoNGNN with two main types of geometric models. The first type integrates high-order SO(3) irreducible representations (including 1-order, i.e., vectors) and mostly employs tensor products to produce equivariant outputs. These models are referred to as equivariant models, including PaiNN (Schütt et al., 2021), MACE (Batatia et al., 2022), Allegro (Musaelian et al., 2023), NequIP (Batzner et al., 2022), Equiformer (Liao & Smidt, 2022). The second type integrates high-order invariant geometry, such as angle, dihedral angle, or learned representations. We refer to these models as invariant models, including DimeNet (Gasteiger et al., 2019), GemNet (Gasteiger et al., 2021) and 2-F-DisGNN (Li et al., 2023b). Note that all of these models can capture high-order geometry, enabling them to achieve state-of-the-art performance on geometric structure learning tasks.

Given that GeoNGNN can be regarded as the subgraph-enhanced version of Vanilla DisGNN, we also implement and evaluate Vanilla DisGNN, which includes more complicated residual layers than its special case SchNet (Schütt et al., 2018), as a baseline to assess the direct improvement achieved through subgraph representation.

Detailed experimental settings are provided in Appendix C.

<sup>4</sup>Despite theoretical completeness, experimental performance may still be hindered by numerical errors, thus failing to distinguish pairs of geometric graphs experimentally.

<sup>5</sup>“Practical” means that in experiments we leverage local message passing and finite subgraph size for tractability and scalability.

## 6.1. Separation Power: Synthetic Counterexamples

We constructed an expressiveness dataset based on counterexamples proposed by Li et al. (2023b) to evaluate the separation power of practical models. The synthetic dataset comprises 10 isolated and 7 combinatorial counterexamples. Each counterexample consists of a pair of highly symmetric geometric graphs that are non-E(3)-isomorphic but indistinguishable by Vanilla DisGNN.

As observed in Table 2, SchNet and Vanilla DisGNN both fail to distinguish any counterexample, while the remaining models all effectively discriminate between all pairs, which aligns with our theoretical findings. Indeed, these results suggest that as long as models incorporate some higher-order geometry than distance, they can possess the ability to differentiate the carefully designed corner cases by Li et al. (2023b), implying that 3D isomorphism problem is much easier than the classical one.

## 6.2. Molecule Structure Learning: Revised MD17

We further evaluate the geometric learning ability of GeoNGNN on the rMD17 dataset (Chmiela et al., 2017), which poses a substantial challenge to models’ geometric expressiveness and generalization power. This dataset encompasses trajectories from molecular dynamics simulations of several small molecules. The objective is to predict the energy and atomic forces of a given molecule conformer which contains all atoms’ positions and atomic numbers.

There are several important observations, as depicted in Table 1: 1) GeoNGNN exhibits substantial improvements over Vanilla DisGNN. The ratio of the loss for GeoNGNN to that of Vanilla DisGNN averages 1:8 and reaches a maximum of 1:37. 2) Though also being E(3)-complete, DimeNet and GemNet show worse performance than GeoNGNN. This finding suggests that different model designs can exhibit different inductive biases, while learning more refined subgraph (local environment) representations may be superior to directional message passing in certain molecule-relevant tasks. 3) GeoNGNN shows competitive performance on the majority of molecules in comparison to other well-designed state-of-the-art models. However, it does not achieve SOTA performance, which may be due to its simple design, leveraging distance only, and the weak base GNN it adopts.

## 6.3. Scaling to Large Graph Size: MD22

A significant concern for geometric models is the scalability for larger geometric graphs. In this subsection, we show that GeoNGNN, though simple, can achieve high performance on relatively large molecules (Chmiela et al., 2023), while exhibiting much faster speed than current SOTA models.

As presented in Table 3 in Appendix B.3, GeoNGNN out-

Table 1. MAE loss on revised MD17. Energy (E) in kcal/mol, force (F) in kcal/mol/Å. We color the cell if GeoNGNN outperforms Vanilla DisGNN. The average rank is the average of the rank of each row.

Mol	Target	Equivariant models				Scalar models				
		PaiNN	Allegro	NequIP	MACE	DimeNet	GemNet	2F-Dis.	Vanilla Dis.	GeoNGNN
aspirin	E	0.1591	0.0530	0.0530	0.0507	0.1321	-	<b>0.0465</b>	0.1348	<u>0.0490</u>
	F	0.3713	0.1683	0.1891	<u>0.1522</u>	0.3549	0.2191	<b>0.1515</b>	0.4468	<u>0.1733</u>
azobenzene	E	-	<u>0.0277</u>	<b>0.0161</b>	<u>0.0277</u>	0.1063	-	0.0315	0.2997	0.0301
	F	-	<b>0.0600</b>	<u>0.0669</u>	0.0692	0.2174	-	0.1121	0.5814	0.1206
benzene	E	-	0.0069	<b>0.0009</b>	0.0092	0.0061	-	<u>0.0013</u>	0.0634	0.0018
	F	-	<b>0.0046</b>	0.0069	<u>0.0069</u>	0.0170	0.0115	0.0085	0.3055	0.0083
ethanol	E	0.0623	0.0092	0.0092	0.0092	0.0345	-	<b>0.0065</b>	0.0129	<u>0.0090</u>
	F	0.2306	<u>0.0484</u>	0.0646	0.0484	0.1859	0.0830	<b>0.0379</b>	0.0825	0.0616
malonaldehyde	E	0.0899	<u>0.0138</u>	0.0184	0.0184	0.0507	-	<b>0.0129</b>	0.0329	0.0145
	F	0.3182	<u>0.0830</u>	0.1176	0.0945	0.2743	0.1522	<b>0.0782</b>	0.1922	0.0923
naphthalene	E	0.1176	<b>0.0046</b>	0.0208	0.0115	0.0445	-	0.0103	0.1496	<u>0.0083</u>
	F	0.0830	<b>0.0208</b>	<u>0.0300</u>	0.0369	0.1105	0.0438	0.0478	0.4608	<u>0.0437</u>
paracetamol	E	-	0.0346	0.0323	<b>0.0300</b>	0.1176	-	<u>0.0310</u>	0.2457	0.0426
	F	-	<u>0.1130</u>	0.1361	<b>0.1107</b>	0.3028	-	0.1178	0.5393	0.1612
salicylic acid	E	0.1130	0.0208	<b>0.0161</b>	0.0208	0.0590	-	0.0174	0.0800	<u>0.0165</u>
	F	0.2099	<b>0.0669</b>	0.0922	<u>0.0715</u>	0.2428	0.1222	0.0860	0.3703	<u>0.0897</u>
toluene	E	0.0969	0.0092	<u>0.0069</u>	0.0115	0.0228	-	<b>0.0051</b>	0.0507	0.0087
	F	0.1015	0.0415	0.0369	<u>0.0346</u>	0.1085	0.0507	<b>0.0284</b>	0.2296	0.0424
uracil	E	0.1038	0.0138	<b>0.0092</b>	0.0115	0.0338	-	0.0139	0.0381	<u>0.0108</u>
	F	0.1407	<b>0.0415</b>	0.0715	<u>0.0484</u>	0.1634	0.0876	0.0828	0.2331	<u>0.0716</u>
AVG RANK		7.79	2.55	3.30	2.90	6.70	6.00	2.70	7.45	3.50

Table 2. The separation results on the constructed dataset.

	SchNet	Vanilla Dis.	DimeNet	PaiNN	MACE	GeoNGNN
Isolated (10 cases)	0%	0%	100%	100%	100%	100%
Combin. (7 cases)	0%	0%	100%	100%	100%	100%

performs Vanilla DisGNN across almost all targets. It exhibits competitive results and achieves several new SOTA results on Stachyose and the two largest molecules, Buckycatcher and Double-walled nanotube. On average, GeoNGNN performs better than all the equivariant models except for MACE, ranking the 2nd among all models.

We further evaluated the inference time and GPU memory consumption of GeoNGNN and several high-performance models. As shown in Table 4 in Appendix B.3, GeoNGNN is more than 2x faster than MACE and more than 8x faster than Equiformer, which both utilize high-order equivariant representations and perform tensor products. Additionally, GeoNGNN demonstrates efficient memory usage, particularly when compared to 2-F-DisGNN and Equiformer.

#### 6.4. Effect of Subgraph Size

In this section, we delve into the impact of subgraph size, which serves as a form of receptive field for each node. Theoretically, a larger receptive field, facilitated by distance encoding, should always result in the same or better expressiveness. To explore how subgraph size affects experimental performance, we selected three molecules of different representative scales and observed the effects, as depicted in Figure 7 in Appendix B.3. As anticipated, performance generally improves with increased subgraph size, roughly matching the improved theoretical expressiveness. How-

ever, the rule does not always hold: there are cases where increasing the subgraph size leads to degraded performance, which can be attributed to the potential noise and redundant information. It implies that there exists a conflict between theoretical expressiveness and experimental performance, and striking a balance between them is important.

## 7. Conclusion and Limitation

**Conclusion.** In this paper, we throughoutly analyze a wide range of invariant models’ theoretical expressiveness. Specifically, we rigorously characterize the expressiveness of Vanilla DisGNN, showcasing that all its unidentifiable cases are highly symmetric graphs with only one global anchor. We then introduce GeoNGNN capable of breaking such symmetry utilizing local anchors which achieves E(3)-completeness. We leverage GeoNGNN as a tool to prove the E(3)-completeness of three well-known invariant models, DimeNet, GemNet and SphereNet, for the first time. Experiments show the competitive performance and faster speed of GeoNGNN compared to geometric models using high-order invariant and equivariant representations.

**Limitation.** The E(3) completeness proof for invariant models are under the assumption of global message passing, i.e., the geometric graphs are fully connected. However, the extent to which these models can exhibit high expressiveness on general sparse graphs remains an open question that needs further investigation. Additionally, future research is needed to characterize the expressiveness of vector models that rely solely on 1-order equivariant representations, which have shown promising experimental results but lack a guarantee of completeness.

## 8. Impact Statements

This paper contributes by characterizing the theoretical expressiveness of invariant geometric models, with the goal of helping researchers better understand the potential and limits of existing geometric models and develop better geometric models for downstream tasks that are beneficial for scientific development. There are many potential societal consequences of our work, none of which we feel must be specifically highlighted here.

## References

- Abou-Rjeili, A. and Karypis, G. Multilevel algorithms for partitioning power-law graphs. In *Proceedings 20th IEEE International Parallel & Distributed Processing Symposium*, pp. 10–pp. IEEE, 2006.
- Adams, K., Pattanaik, L., and Coley, C. W. Learning 3d representations of molecular chirality with invariance to bond rotations. In *International Conference on Learning Representations*, 2021.
- Batatia, I., Kovacs, D. P., Simm, G., Ortner, C., and Csányi, G. Mace: Higher order equivariant message passing neural networks for fast and accurate force fields. *Advances in Neural Information Processing Systems*, 35: 11423–11436, 2022.
- Batzner, S., Musaelian, A., Sun, L., Geiger, M., Mailoa, J. P., Kornbluth, M., Molinari, N., Smidt, T. E., and Kozinsky, B. E (3)-equivariant graph neural networks for data-efficient and accurate interatomic potentials. *Nature communications*, 13(1):1–11, 2022.
- Bevilacqua, B., Frasca, F., Lim, D., Srinivasan, B., Cai, C., Balamurugan, G., Bronstein, M. M., and Maron, H. Equivariant subgraph aggregation networks. In *International Conference on Learning Representations*, 2021.
- Brandstetter, J., Hesselink, R., van der Pol, E., Bekkers, E. J., and Welling, M. Geometric and physical quantities improve e (3) equivariant message passing. In *International Conference on Learning Representations*, 2021.
- Cai, J.-Y., Fürer, M., and Immerman, N. An optimal lower bound on the number of variables for graph identification. *Combinatorica*, 12(4):389–410, 1992.
- Chmiela, S., Tkatchenko, A., Sauceda, H. E., Poltavsky, I., Schütt, K. T., and Müller, K.-R. Machine learning of accurate energy-conserving molecular force fields. *Science advances*, 3(5):e1603015, 2017.
- Chmiela, S., Vassilev-Galindo, V., Unke, O. T., Kabylda, A., Sauceda, H. E., Tkatchenko, A., and Müller, K.-R. Accurate global machine learning force fields for molecules with hundreds of atoms. *Science Advances*, 9(2):eadf0873, 2023.
- Degen, J., Wegscheid-Gerlach, C., Zaliani, A., and Rarey, M. On the art of compiling and using ‘drug-like’ chemical fragment spaces. *ChemMedChem: Chemistry Enabling Drug Discovery*, 3(10):1503–1507, 2008.
- Delle Rose, V., Kozachinskiy, A., Rojas, C., Petrache, M., and Barceló, P. Three iterations of  $(d - 1)$ -wl test distinguish non isometric clouds of  $d$ -dimensional points. *arXiv e-prints*, pp. arXiv–2303, 2023.
- Deng, C., Litany, O., Duan, Y., Poulenard, A., Tagliasacchi, A., and Guibas, L. J. Vector neurons: A general framework for so (3)-equivariant networks. In *Proceedings of the IEEE/CVF International Conference on Computer Vision*, pp. 12200–12209, 2021.
- Duval, A. A., Schmidt, V., Hernández-García, A., Miret, S., Malliaros, F. D., Bengio, Y., and Rolnick, D. Faenet: Frame averaging equivariant gnn for materials modeling. In *International Conference on Machine Learning*, pp. 9013–9033. PMLR, 2023.
- Dym, N. and Maron, H. On the universality of rotation equivariant point cloud networks. In *International Conference on Learning Representations*, 2020.
- Fey, M. and Lenssen, J. E. Fast graph representation learning with pytorch geometric. *arXiv preprint arXiv:1903.02428*, 2019.
- Frasca, F., Bevilacqua, B., Bronstein, M., and Maron, H. Understanding and extending subgraph gnns by rethinking their symmetries. *Advances in Neural Information Processing Systems*, 35:31376–31390, 2022.
- Fuchs, F., Worrall, D., Fischer, V., and Welling, M. Se (3)-transformers: 3d roto-translation equivariant attention networks. *Advances in Neural Information Processing Systems*, 33:1970–1981, 2020.
- Gaiński, P., Koziarski, M., Tabor, J., and Śmieja, M. Chien: Embracing molecular chirality with graph neural networks. In *Joint European Conference on Machine Learning and Knowledge Discovery in Databases*, pp. 36–52. Springer, 2023.
- Gasteiger, J., Groß, J., and Günnemann, S. Directional message passing for molecular graphs. In *International Conference on Learning Representations*, 2019.
- Gasteiger, J., Giri, S., Margraf, J. T., and Günnemann, S. Fast and uncertainty-aware directional message passing for non-equilibrium molecules. *arXiv preprint arXiv:2011.14115*, 2020.

- Gasteiger, J., Becker, F., and Günnemann, S. Gemnet: Universal directional graph neural networks for molecules. In Ranzato, M., Beygelzimer, A., Dauphin, Y., Liang, P., and Vaughan, J. W. (eds.), *Advances in Neural Information Processing Systems*, volume 34, pp. 6790–6802. Curran Associates, Inc., 2021. URL <https://proceedings.neurips.cc/paper/2021/file/35cf8659cfcb13224cbd47863a34fc58-Paper.pdf>.
- Gasteiger, J., Shuaibi, M., Sriram, A., Günnemann, S., Ulissi, Z. W., Zitnick, C. L., and Das, A. Gemnet-oc: Developing graph neural networks for large and diverse molecular simulation datasets. *Transactions on Machine Learning Research*, 2022.
- Gilmer, J., Schoenholz, S. S., Riley, P. F., Vinyals, O., and Dahl, G. E. Neural message passing for quantum chemistry. In *International conference on machine learning*, pp. 1263–1272. PMLR, 2017.
- Guo, Y., Wang, H., Hu, Q., Liu, H., Liu, L., and Bennamoun, M. Deep learning for 3d point clouds: A survey. *IEEE transactions on pattern analysis and machine intelligence*, 43(12):4338–4364, 2020.
- Han, J., Rong, Y., Xu, T., and Huang, W. Geometrically equivariant graph neural networks: A survey. 2022.
- Hordan, S., Amir, T., Gortler, S. J., and Dym, N. Complete neural networks for euclidean graphs. *arXiv preprint arXiv:2301.13821*, 2023.
- Hornik, K., Stinchcombe, M., and White, H. Multilayer feedforward networks are universal approximators. *Neural networks*, 2(5):359–366, 1989.
- Jumper, J., Evans, R., Pritzel, A., Green, T., Figurnov, M., Ronneberger, O., Tunyasuvunakool, K., Bates, R., Žídek, A., Potapenko, A., et al. Highly accurate protein structure prediction with alphafold. *Nature*, 596(7873):583–589, 2021.
- Kingma, D. P. and Ba, J. Adam: A method for stochastic optimization. *arXiv preprint arXiv:1412.6980*, 2014.
- Kovacs, D. P., Batatia, I., Arany, E. S., and Csanyi, G. Evaluation of the mace force field architecture: from medicinal chemistry to materials science. *arXiv preprint arXiv:2305.14247*, 2023.
- Li, Y., Wang, Y., Huang, L., Yang, H., Wei, X., Zhang, J., Wang, T., Wang, Z., Shao, B., and Liu, T.-Y. Long-short-range message-passing: A physics-informed framework to capture non-local interaction for scalable molecular dynamics simulation. *arXiv preprint arXiv:2304.13542*, 2023a.
- Li, Z., Wang, X., Huang, Y., and Zhang, M. Is distance matrix enough for geometric deep learning? *Advances in Neural Information Processing Systems*, 2023b.
- Liao, Y.-L. and Smidt, T. Equiformer: Equivariant graph attention transformer for 3d atomistic graphs. In *The Eleventh International Conference on Learning Representations*, 2022.
- Liu, Y., Wang, L., Liu, M., Lin, Y., Zhang, X., Oztekin, B., and Ji, S. Spherical message passing for 3d molecular graphs. In *International Conference on Learning Representations*, 2021.
- Maron, H., Ben-Hamu, H., Shamir, N., and Lipman, Y. Invariant and equivariant graph networks. In *International Conference on Learning Representations*, 2018.
- Morris, C., Ritzert, M., Fey, M., Hamilton, W. L., Lenssen, J. E., Rattan, G., and Grohe, M. Weisfeiler and leman go neural: Higher-order graph neural networks. In *Proceedings of the AAAI conference on artificial intelligence*, volume 33, pp. 4602–4609, 2019.
- Musaelian, A., Batzner, S., Johansson, A., Sun, L., Owen, C. J., Kornbluth, M., and Kozinsky, B. Learning local equivariant representations for large-scale atomistic dynamics. *Nature Communications*, 14(1):579, 2023.
- Pattanaik, L., Ganea, O.-E., Coley, I., Jensen, K. F., Green, W. H., and Coley, C. W. Message passing networks for molecules with tetrahedral chirality, 2020.
- Pozdnyakov, S. N. and Ceriotti, M. Incompleteness of graph convolutional neural networks for points clouds in three dimensions. *arXiv preprint arXiv:2201.07136*, 2022.
- Puny, O., Atzmon, M., Smith, E. J., Misra, I., Grover, A., Ben-Hamu, H., and Lipman, Y. Frame averaging for invariant and equivariant network design. In *International Conference on Learning Representations*, 2021.
- Qian, C., Rattan, G., Geerts, F., Niepert, M., and Morris, C. Ordered subgraph aggregation networks. *Advances in Neural Information Processing Systems*, 35:21030–21045, 2022.
- Sanchez-Gonzalez, A., Godwin, J., Pfaff, T., Ying, R., Leskovec, J., and Battaglia, P. Learning to simulate complex physics with graph networks. In *International Conference on Machine Learning*, pp. 8459–8468. PMLR, 2020.
- Satorras, V. G., Hoogeboom, E., and Welling, M. E (n) equivariant graph neural networks. In *International conference on machine learning*, pp. 9323–9332. PMLR, 2021.

- Schmitz, G., Godtliebsen, I. H., and Christiansen, O. Machine learning for potential energy surfaces: An extensive database and assessment of methods. *The Journal of chemical physics*, 150(24):244113, 2019.
- Schütt, K., Unke, O., and Gastegger, M. Equivariant message passing for the prediction of tensorial properties and molecular spectra. In *International Conference on Machine Learning*, pp. 9377–9388. PMLR, 2021.
- Schütt, K. T., Sauceda, H. E., Kindermans, P.-J., Tkatchenko, A., and Müller, K.-R. Schnet—a deep learning architecture for molecules and materials. *The Journal of Chemical Physics*, 148(24):241722, 2018.
- Thölke, P. and De Fabritiis, G. Equivariant transformers for neural network based molecular potentials. In *International Conference on Learning Representations*, 2021.
- Thomas, N., Smidt, T., Kearnes, S., Yang, L., Li, L., Kohlhoff, K., and Riley, P. Tensor field networks: Rotation-and translation-equivariant neural networks for 3d point clouds. *arXiv preprint arXiv:1802.08219*, 2018.
- Wang, X. and Zhang, M. Graph neural network with local frame for molecular potential energy surface. In *Learning on Graphs Conference*, pp. 19–1. PMLR, 2022.
- Weisfeiler, B. and Leman, A. The reduction of a graph to canonical form and the algebra which appears therein. *NTI, Series*, 2(9):12–16, 1968.
- Xu, K., Hu, W., Leskovec, J., and Jegelka, S. How powerful are graph neural networks? In *International Conference on Learning Representations*, 2018.
- Zaheer, M., Kottur, S., Ravanbakhsh, S., Poczos, B., Salakhutdinov, R. R., and Smola, A. J. Deep sets. *Advances in Neural Information Processing Systems*, 30, 2017.
- Zhang, B., Feng, G., Du, Y., He, D., and Wang, L. A complete expressiveness hierarchy for subgraph gnns via subgraph weisfeiler-lehman tests. *arXiv preprint arXiv:2302.07090*, 2023.
- Zhang, M. and Li, P. Nested graph neural networks. *Advances in Neural Information Processing Systems*, 34: 15734–15747, 2021.
- Zhao, L., Jin, W., Akoglu, L., and Shah, N. From stars to subgraphs: Uplifting any gnn with local structure awareness. In *International Conference on Learning Representations*, 2021.

## A. Extended Analysis of Vanilla DisGNN

### A.1. Stronger Necessary Condition for Unidentifiable Cases

In the case of geometric graphs where all node features are identical, such as raw point clouds, the global anchor set naturally degenerates, as shown in the left figure of Figure 4. As a consequence, based on the necessary condition 3.5, we cannot determine whether these geometric graphs can be identified by Vanilla DisGNN. Here, we define two higher-level symmetries, i.e.,  $GA^C$ - and  $GA^{\mathcal{V}\mathcal{D}}$ -symmetry, of a given geometric graph  $G$  and, therefore, enhance the necessary condition to finely bound the expressiveness of Vanilla DisGNN, as illustrated in Figure 2.

We first define an *enlarged global anchor set* on a given graph  $G$  through the graphs' spatial environments. Formally, we first use some permutation-equivariant and E(3)-invariant algorithm  $\mathcal{S}(G) : \mathbb{R}^{n \times d} \times \mathbb{R}^{n \times 3} \rightarrow \mathbb{R}^{n \times d_{pre}}$  to extract nodes' spatial features from their environments as a pre-processing. These spatial features are then fused with the nodes' initial features using an injective function, resulting in the *enhanced node features*. Subsequently, the mass function  $m$  is applied to the graph  $G$  but with enhanced node features to calculate the anchor.

We denote the resulting global anchor as  $A^{\mathcal{S},m}(G)$ , and use  $\mathbf{A}^{\mathcal{S}}(G)$  to denote the corresponding set. Accordingly, we define graph  $G$  to be  **$GA^{\mathcal{S}}$ -symmetric** if  $|\mathbf{A}^{\mathcal{S}}(G)| = 1$ .

It should be emphasized that  $\mathbf{A}(G) \subseteq \mathbf{A}^{\mathcal{S}}(G)$  for all  $\mathcal{S}$  and  $G$ , as the use of  $\mathcal{S}$  always results in a no-coarser node individualization, and therefore,  $GA^{\mathcal{S}}$ -symmetric  $\Rightarrow$   $GA$ -symmetric, meaning that  $GA^{\mathcal{S}}$ -symmetry always represents a higher-level symmetry than  $GA$ -symmetry.

We introduce two simple types of color refinement algorithms that effectively generate more global anchors, and more importantly, these refinement algorithms can both *be performed by Vanilla DisGNN automatically*:

- Center enhancement  $\mathcal{C}$ , which enhances node features by incorporating the distance of each node to the geometric center. See Figure 4 for illustration.
- Vanilla DisGNN enhancement  $\mathcal{V}\mathcal{D}$ , which refines node features by applying Vanilla DisGNN onto the graph. It is important to note that Vanilla DisGNN here is used as a color refinement algorithm, and different parameterizations (as long as they satisfy the injective assumption) will yield the same individualization of node features, thus the same  $\mathbf{A}^{\mathcal{V}\mathcal{D}}(G)$ .

By taking a geometric graph  $G$  as input, Vanilla DisGNN is able to learn to perform APE related to the largest global anchor set  $\mathbf{A}^{\mathcal{V}\mathcal{D}}(G)$  *automatically*:

**Proposition A.1.** (*Locate Enhanced Global Anchors*) *Given a geometric graph  $G$ , denote node  $i$ 's representation produced by infinite-round Vanilla DisGNN as  $h_i$ , then we have:*

- (*Inclusion relation*)  $\mathbf{A}^{\mathcal{C}}(G) \subseteq \mathbf{A}^{\mathcal{V}\mathcal{D}}(G)$
- (*Node-GA distance*) For an arbitrary mass function  $m$ ,  $h_i$  can derive  $d_{i, \mathbf{A}^{\mathcal{V}\mathcal{D}}, m}$ .
- (*GA-GA distance*) For arbitrary two mass functions  $m_1$  and  $m_2$ ,  $\{h_i \mid i \in [n]\}$  can derive  $d_{\mathbf{A}^{\mathcal{V}\mathcal{D}}, m_1, \mathbf{A}^{\mathcal{V}\mathcal{D}}, m_2}$ .
- (*Counting enhanced GA*)  $\{h_i^{(2)} \mid i \in [n]\}$  can derive  $\mathbb{1}_{|\mathbf{A}^{\mathcal{V}\mathcal{D}}(G)|=1}$ .

Proposition A.1 is the enhanced version of Proposition 3.2, demonstrating that Vanilla DisGNN possesses the geometric capability to acquire global geometric information not only w.r.t. global anchors defined on initial node features but also w.r.t. the enhanced global anchors defined on  $\mathcal{V}\mathcal{D}$  enhanced node features. In practice, there is no necessity for an infinite number of rounds. Instead, the process can terminate when the equivalence partition of features is not further refined, and with two more rounds of Vanilla DisGNN, the global geometric information can be extracted.

We note that the first conclusion of Proposition A.1 implies that  $GA^{\mathcal{V}\mathcal{D}} \Rightarrow GA^{\mathcal{C}}$ , suggesting that  $GA^{\mathcal{V}\mathcal{D}}$  is a higher-level symmetry. Consequently, the space in which graphs exhibit  $GA^{\mathcal{V}\mathcal{D}}$ -symmetry is a subset of the space of  $GA^{\mathcal{C}}$ -symmetric graphs. Furthermore, we can demonstrate that the space of  $GA^{\mathcal{V}\mathcal{D}}$ -symmetric graphs is **strictly** contained within the space of  $GA^{\mathcal{C}}$ -symmetric graphs. This is because there exist geometric graphs that display  $GA^{\mathcal{C}}$ -symmetry but not  $GA^{\mathcal{V}\mathcal{D}}$ -symmetry, as illustrated in Figure 3.

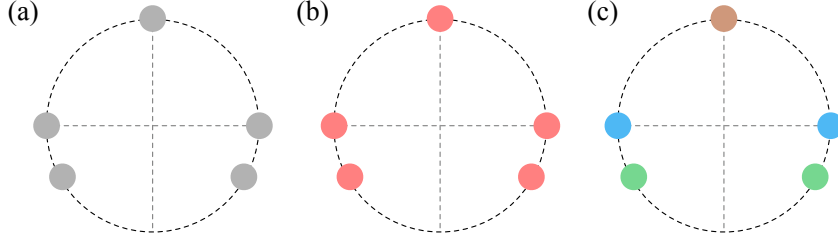


Figure 3. A geometric graph  $G$  that exhibits  $GA^C$ -symmetry but not  $GA^{VD}$ -symmetry. (a) The geometric graph  $G$ , consisting of an equilateral triangle and two additional nodes. (b) The graph  $G$  after center enhancement. Note that each node has the same distance to the geometric center, therefore the nodes still remain undivided. (c) The graph  $G$  after Vanilla DisGNN enhancement.

Consequently, we can prove the following stronger necessary condition:

**Theorem A.2.** (Necessary condition for unidentifiable cases) *Given a geometric graph  $G$ , Vanilla DisGNN cannot identify  $G$  only if  $G$  is  $GA^{VD}$ -symmetric.*

Condition A.2 demonstrates that all unidentifiable cases by Vanilla DisGNN are  $GA^{VD}$ -symmetric, a much higher-level symmetry. Therefore, we further restrict the unidentifiable cases into a much smaller geometric graph subspace, illustrated in Figure 2.

With such a condition, we can determine more geometric graphs that Vanilla DisGNN can identify. For example, with the weaker necessary condition 3.5 shown in the main body, we do not know whether the left-most geometric graphs in Figure 3 and Figure 4 are identifiable by Vanilla DisGNN, since they are all  $GA$ -symmetric. However, we can now determine they are identifiable indeed, since the graph in Figure 3 is not  $GA^{VD}$ -symmetric, and the graph in Figure 4 is even not  $GA^C$ -symmetric.

At last, we demonstrate that there exist geometric graphs that are  $GA^{VD}$ -symmetric but can be identified by Vanilla DisGNN. Specifically, we establish that the relationship between the red and purple subspaces in Figure 2 can be accurately described as a *proper subset*. To illustrate this, let us consider an equilateral triangle of arbitrary length without any initial node features as the base geometric graph  $G$  (i.e., the left-most figure in Figure 1). For any other geometric graph  $G'$  that is non-E(3)-isomorphic to  $G$ , we encounter only three scenarios: (1)  $G'$  has a different number of nodes than 3, (2)  $G'$  consists of 3 nodes forming an equilateral triangle but with a distinct length, or (3)  $G'$  consists of 3 nodes arranged in a manner that does not form an equilateral triangle. Importantly, Vanilla DisGNN possesses the capability to distinguish between  $G$  and  $G'$  for all three cases, due to its ability to embed node numbers and all distance lengths. Consequently, Vanilla DisGNN successfully identifies  $G$ . However,  $G$  is  $GA^{VD}$ -symmetric, as all three nodes are isomorphic at the node-level.

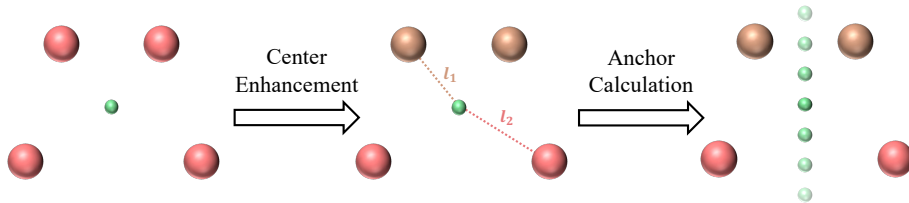


Figure 4. Center enhancement for the global anchor set. Prior to the enhancement, the global anchor set degenerates into a single point, i.e.,  $|\mathbf{A}(G)| = 1$ . After the enhancement, the global anchor set expands to form a line with an infinite number of anchors, i.e.,  $|\mathbf{A}^C(G)| > 1$ .

## A.2. Assessment of Symmetric Graphs on Real-World Datasets

In this subsection, we perform assessments on real-world datasets with the objective of addressing the following question: *What is the proportion of unidentifiable cases for Vanilla DisGNN in real-world geometric graphs?* We answer this question by assessing the proportion of unidentifiable cases' supersets, namely  $GA$ -,  $GA^C$ - and  $GA^C$ -symmetric geometric graphs, and therefore indirectly assessing the proportion of unidentifiable cases. Our findings demonstrate that, theoretically, Vanilla DisGNN can identify *nearly all* geometric graphs present in real-world datasets.

We first give a proposition, which can determine whether a given geometric graph is  $GA$ -symmetric in finite-step without

the need to iterate all mass functions  $m$ :

**Proposition A.3.** (*Degeneration of Global Anchor Set*) Given an arbitrary geometric graph  $G = (X, P)$ , let  $K$  denote the number of distinct node features, i.e.,  $|\{X_i \mid i \in [n]\}| = K$ , and let  $X_k^*$  represent the  $k$ -th type of node features. Then we have:  $G$  is GA-symmetric  $\iff$  all  $X_k^*$ -type geometric centers of  $G$  coincide.

Note that  $GA^S$ -symmetry of a given geometric graph  $G$  can also be readily determined using Proposition A.3, with the only distinction being that  $X_k^*$  defined on the enhanced node features.

Next, we outline several evaluation criteria that serve as guidelines for determining whether a given geometric graph is symmetric in real-world datasets.

**Evaluation criteria.** In the context of real-world geometric graphs, it is pertinent to acknowledge the presence of inherent coordinate noise, which renders them deviant from being inherently symmetric in an ideal sense. Additionally, computational calculations are subjected to floating-point errors. Accordingly, we propose the introduction of two tolerance errors that govern the sensitivity of the aforementioned noise and errors when determining whether a geometric graph is symmetric: 1) The **rounding number**  $r$  for distance-related enhancement. During  $\mathcal{C}$ - or  $\mathcal{VD}$ -enhancement, we augment node features by incorporating distance information. We round the distance values to  $r$  decimal places for more insensitive to noise. 2) The **deviation error**  $\epsilon$ . In order to ascertain the symmetry of a graph, Proposition A.3 is employed. Accounting for errors, a geometric graph is considered symmetric if all the type-centers are located within a ball centered at the type-centers' center, with a radius of  $\epsilon$ .

Note that *the lower the rounding number or the larger the deviation error, the less sensitive the criteria is to noise*. As a consequence, there is a *higher likelihood* of a graph being determined as symmetric.

**Real-world datasets.** We select two representative datasets, namely QM9 and ModelNet, for the assessment. The QM9 dataset comprises approximately 130K molecules, while the ModelNet dataset consists of roughly 12K real-world point clouds categorized into 40 classes, including objects such as chairs, beds, and more. Both datasets encompass numeric geometric graphs, and our objective is to count the occurrence of symmetric graphs within them. Notably, in the case of the ModelNet dataset, initial node features are absent, resulting in all graphs being inherently GA-symmetric, as we demonstrated previously. However, they may not necessarily exhibit  $GA^C$ -symmetry, therefore can further be identifiable cases of Vanilla DisGNN.

**Rescaling and criteria settings.** Since the two datasets under consideration exhibit different scales, making the use of fixed tolerance errors inapplicable. To address this, a preprocessing step is performed on both datasets by **rescaling** all geometric graphs to ensure that the distance between the geometric center and the farthest node is 1. We then fix the rounding number to 2 for QM9 and 1 for ModelNet (which is quite robust against noise in this scale), and conduct the assessment with the deviation error ranging from  $1e-6$  to  $1e-1$ . Note that a deviation error of  $1e-1$  is quite large for a geometric graph located within a unit sphere. As a result, many non-symmetric graphs may still be identified as symmetric under such criteria. We use this as a rough upper bound only for reference.

**Results.** The assessment results in Figure 5 reveal the following observations: 1) Concerning the QM9 dataset, even when utilizing the largest deviation error ( $1e-1$ ), the proportion of  $GA^C$ - and  $GA^{\mathcal{VD}}$ -symmetric geometric graphs are less than  $\sim 0.1\%$  of the entire dataset. Since  $GA^C$ - and  $GA^{\mathcal{VD}}$ -symmetric geometric graph spaces are supersets of the unidentifiable space of Vanilla DisGNN, therefore the unidentifiable proportion can only be less than  $\sim 0.1\%$ . When considering a relatively stricter deviation error ( $1e-2$ ), even the simplest symmetric graphs, i.e., GA-symmetric graphs, amount to less than  $\sim 0.25\%$  of the whole dataset. With the strictest deviation error, only 0.0046% of the graphs (6 out of  $\sim 130K$ ) exhibit symmetry across all symmetric types. 2) In the ModelNet dataset, as anticipated, all the geometric graphs inherently possess GA-symmetry. However, when deviation error is less than  $1e-1$ , only 1 or 2 geometric graphs demonstrate  $GA^C$ -symmetry. And there is no  $GA^{\mathcal{VD}}$ -symmetric graphs found across all deviation errors.

To summarize, the statistical results imply that the occurrence of unidentifiable graphs of Vanilla DisGNN is **exceedingly rare and practically negligible** in real-world scenarios.

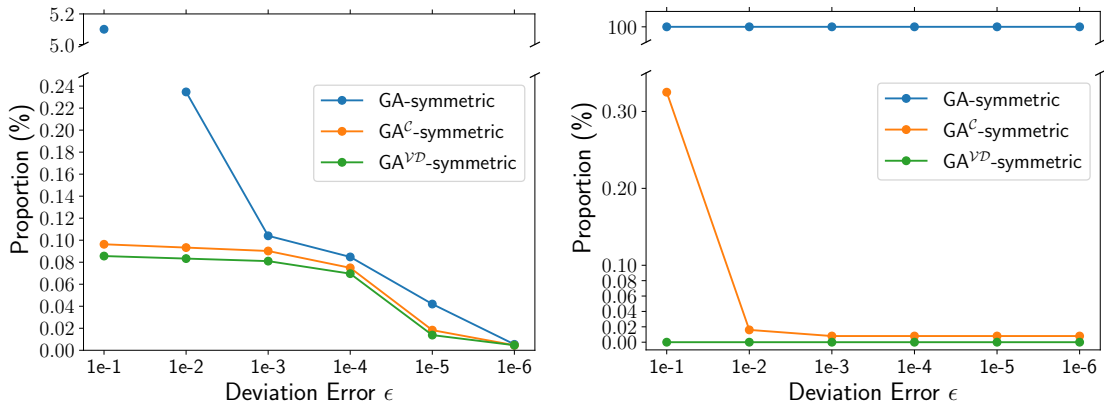


Figure 5. Assessment of symmetric geometric graphs in real-world datasets. (a) Proportion of symmetric geometric graphs in the QM9 dataset. (b) Proportion of symmetric geometric graphs in the ModelNet dataset. The proportions of  $GA^{V^D}$ -symmetric geometric graphs in ModelNet is zero across all deviation errors.

## B. Supplementary Analysis for GeoNGNN

### B.1. Complexity Analysis

Without considering the complexity of achieving injective intermediate functions, GeoNGNN achieves theoretical completeness with an asymptotic time complexity of  $O(n^3)$ . This complexity arises from the fact that there are  $n$  subgraphs, each of which undergoes the complete-version Vanilla DisGNN operation, resulting in an overall complexity of  $O(n^2)$  per subgraph. Importantly, this time complexity is consistent with that of 2-F-DisGNN (Li et al., 2023b), DimeNet (Gasteiger et al., 2019), and SphereNet (Liu et al., 2021), when their conditions for achieving E(3)-completeness is met.

Practical GeoNGNN achieves an asymptotic time complexity of  $O(n)$  by restricting the subgraph cutoff and the message passing cutoff to fixed values. Experiments show that practical GeoNGNN exhibits good inductive bias through capturing local subgraph environments. In the following subsection, we provide a demonstration that practical GeoNGNN also possesses better theoretical expressiveness compared to Vanilla DisGNN.

### B.2. Theoretical Expressiveness with finite subgraph radius

Though in practice we have to set finite subgraph radius for GeoNGNN, this still leads to boosted expressiveness compared to Vanilla DisGNN. We demonstrate this through an example.

Take the left pair of geometric graphs in Figure 8 for example, note that this pair of geometric graphs cannot be distinguished by Vanilla DisGNN. Assuming that the subgraph radius for each node is finite, only covering nodes’ one-hop neighbors, as illustrated in Figure 6. The representation of the green node produced by inner Vanilla DisGNN will differ between the two graphs, due to the presence of long-distance information on the left graph, whereas it is absent on the right graph. Therefore, GeoNGNN with such a small subgraph radius can easily distinguish the two geometric graphs.

### B.3. Supplementary Experiment Information

1. Performance of GeoNGNN on MD22 (Table 3) in Section 6.3.
2. Efficiency analysis (Table 4) in Section 6.3.
3. Subgraph size effect analysis (Figure 7) in Section 6.4.

## C. Detailed Experimental Settings

### C.1. Dataset Settings

**Synthetic dataset.** We generate the synthetic dataset by implementing the counterexamples proposed by Li et al. (2023b).

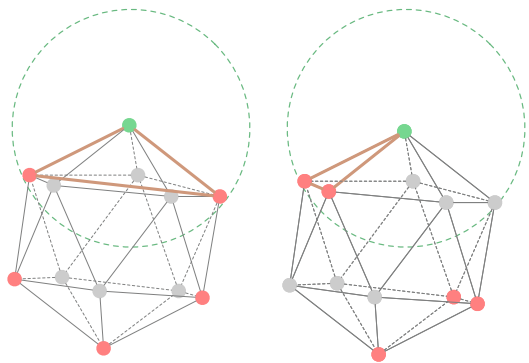


Figure 6. An example that illustrates the separation power of finite-subgraph-size GeoNGNN. The green node represents the central node, while the green *sphere* depicts the subgraph environment surrounding the central node. The brown line signifies the distance information that will be aggregated during the message passing.

Table 3. MAE loss on MD22. Energy (E) in meV/atom, force (F) in meV/Å. We color the cell if GeoNGNN outperforms Vanilla DisGNN. The average rank is the average of the rank of each row. We also show the number of atoms for each molecule.

Molecule	# atoms	Target	sGDML	Equivariant models					Invariant models	
				PaiNN	TorchMD-NET	Allegro	Equiformer	MACE	Vanilla Dis.	GeoNGNN
Ac-Ala3-NHMe	42	E	0.4	0.121	0.116	<u>0.105</u>	0.106	<b>0.064</b>	0.158	0.106
		F	34	10.0	8.1	4.6	3.9	<b>3.8</b>	9.5	4.9
Docosahexaenoic acid	56	E	1	<b>0.089</b>	<u>0.093</u>	<b>0.089</b>	0.214	0.102	0.281	0.105
		F	33	5.9	5.2	3.2	<b>2.5</b>	<u>2.8</u>	11.3	3.8
Stachyose	87	E	2	0.076	<u>0.069</u>	0.124	0.078	<b>0.062</b>	0.077	0.091
		F	29	10.1	8.3	4.2	3.0	3.8	4.1	<b>2.9</b>
AT-AT	60	E	0.52	0.121	0.139	0.103	<u>0.109</u>	<u>0.079</u>	0.085	<b>0.073</b>
		F	30	10.3	8.8	<b>4.1</b>	4.3	<u>4.3</u>	8.463	5.8
AT-AT-CG-CG	118	E	0.52	0.097	0.193	0.145	<b>0.055</b>	<u>0.058</u>	0.082	0.078
		F	31	16.0	20.4	5.6	<u>5.4</u>	<b>5</b>	13.8	8.1
Buckyball catcher	148	E	0.34	-	-	-	-	<u>0.141</u>	0.158	<b>0.113</b>
		F	29	-	-	-	-	<b>3.7</b>	19.3	4.8
Double-walled nanotube	370	E	0.47	-	-	-	-	<b>0.194</b>	0.383	<u>0.204</u>
		F	23	-	-	-	-	12	16.5	<b>11.2</b>
AVG RANK			6.86	5.40	5.30	3.50	3.00	1.79	4.57	2.93

Table 4. Efficiency Analysis of Models. The batch size for all molecules is set to 16, except for Bu and Do where it is 4. Models marked with an asterisk (\*) utilize a batch size of 8, except for Bu and Do, which use a batch size of 2. The evaluation is conducted on Nvidia A100.

Molecule	# atoms	MACE	2F-DisGNN	Equiformer*	GeoNGNN
Ac-Ala3-NHMe	42	0.166	0.130	0.305	<b>0.070</b>
		13400	20542	38895	<b>12997</b>
Docosahexaenoic acid	56	0.209	0.215	0.397	<b>0.088</b>
		17875	35844	51565	<b>16980</b>
Stachyose	87	0.388	OOM	OOM	<b>0.161</b>
		33146	OOM	OOM	<b>32430</b>
AT-AT	60	0.195	0.244	0.361	<b>0.083</b>
		17310	41125	50032	<b>15864</b>
AT-AT-CG-CG	118	0.437	OOM	OOM	<b>0.175</b>
		38090	OOM	OOM	<b>34951</b>
Buckyball catcher	148	0.183	0.382	0.382	<b>0.074</b>
		14466	62790	47702	<b>13891</b>
Double-walled nanotube	370	0.545	OOM	OOM	<b>0.180</b>
		44923	OOM	OOM	<b>36849</b>

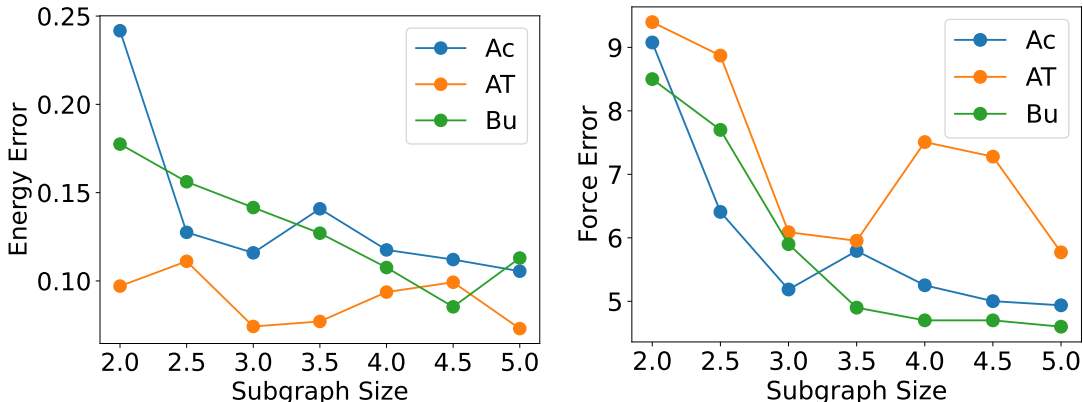


Figure 7. Effect of subgraph size for energy and force prediction on Ac-Ala3-NHMe, AT-AT and Buckyball catcher in MD22. Subgraph size in Å, energy (E) in meV/atom, force (F) in meV/Å.

The dataset includes 10 isolated cases and 7 combinatorial cases, where each case consists of a pair of symmetric geometric graphs that cannot be distinguished by Vanilla DisGNN. Figure 8 shows two pairs of selected counterexamples.

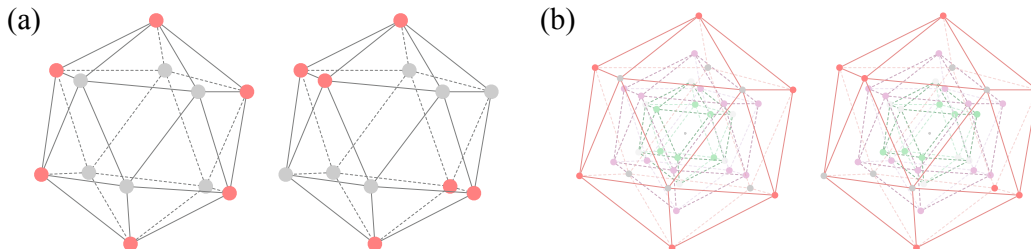


Figure 8. Selected counterexamples in the synthetic dataset. Only colored nodes belong to the geometric graphs. The grey nodes and “edges” are for visualization purposes only. (a) One isolated case. (b) One combinatorial case.

The 10 isolated cases comprise the following: 6 pairs of geometric graphs sampled from regular dodecahedrons, 1 pair from icosahedrons, 2 pairs from a combination of one cube and one regular octahedron, and 1 pair from a combination of two cubes. In the combination cases, the relative size is set to 1/2.

The 7 combinatorial cases are obtained through the augmentation of the 6 pairs of graphs sampled from regular dodecahedrons and 1 pair from icosahedrons, using the method outlined in Theorem A.1 of Li et al. (2023b). When augmenting the base graph, we consider the *original*, *complementary*, and *all* types of the base graph, respectively.

Given that the counterexamples are designed to test the maximal expressiveness of geometric models, we configure all graphs in the dataset to be fully connected.

**rMD17 and MD22.** The data split (training/validation/testing) in rMD17 is 950 / 50 / the rest, following the convention used in related works such as Batatia et al. (2022); Gasteiger et al. (2021). For MD22, we adopt the data split specified in Chmiela et al. (2023), which is also consistent with the other works. We train the models using a batch size of 4.

To optimize the parameters  $\theta$  of the model  $f_\theta$ , we use a weighted loss function:

$$\mathcal{L}(\mathbf{X}, \mathbf{z}) = (1 - \rho)|f_\theta(\mathbf{X}, \mathbf{z}) - \hat{t}(\mathbf{X}, \mathbf{z})| + \frac{\rho}{N} \sum_{i=1}^N \sqrt{\sum_{\alpha=1}^3 \left(-\frac{\partial f_\theta(\mathbf{X}, \mathbf{z})}{\partial \mathbf{x}_{i\alpha}} - \hat{F}_{i\alpha}(\mathbf{X}, \mathbf{z})\right)^2},$$

where  $X \in \mathbb{R}^{N \times 3}$  and  $z \in \mathbb{R}^N$  represents the  $n$  atoms’ coordinates and atomic number respectively,  $\hat{t}$  and  $\hat{F}$  represents the molecule’s energy and forces acting on atoms respectively. The force ratio  $\rho$  is chosen as 0.99 or 0.999.

In rMD17, the experimental results of Allegro (Musaelian et al., 2023), NequIP (Batzner et al., 2022), GemNet (Gasteiger

et al., 2021), are sourced from Musaelian et al. (2023). The result of PaiNN (Schütt et al., 2021) is sourced from Batatia et al. (2022). The results of 2-F-DisGNN (Li et al., 2023b) and MACE (Batatia et al., 2022) are reported by their original papers. We trained and evaluated DimeNet (Gasteiger et al., 2019) using its implementation in Pytorch Geometric (Fey & Lenssen, 2019) and the default parameters (We find that the default parameters produce the best performance).

In MD22, the results of sGDML and MACE (Kovacs et al., 2023) are sourced from Kovacs et al. (2023). The results of PaiNN (Schütt et al., 2021), TorchMD-Net (Thölke & De Fabritiis, 2021), Allegro (Musaelian et al., 2023), and Equiformer (Liao & Smidt, 2022) are obtained from the work presented by Li et al. (2023a).

## C.2. Model Settings.

**RBF.** Following previous work, we use radial basis functions (RBF)  $f_e^{\text{rbf}} : \mathbb{R} \rightarrow \mathbb{R}^{H_{\text{rbf}}}$  to expand the euclidean distance between two nodes into a vector, which is shown to be beneficial for inductive bias Gasteiger et al. (2019); Li et al. (2023b). We use the same nexnorm RBF function like Li et al. (2023b), defined as

$$f_e^{\text{rbf}}(e_{ij})_k = e^{-\beta_k(\exp(-e_{ij}) - \mu_k)^2}, \quad (2)$$

where  $\beta_k, \mu_k$  are coefficients of the  $k^{\text{th}}$  basis.

**Vanilla DisGNN.** In each stage of the Vanilla DisGNN, we augment its expressiveness and experimental performance by stacking dense layers or residual layers, which together with summation aggregation essentially forming the multiset function described in Xu et al. (2018). Vanilla DisGNN’s architecture is described in Figure 9.

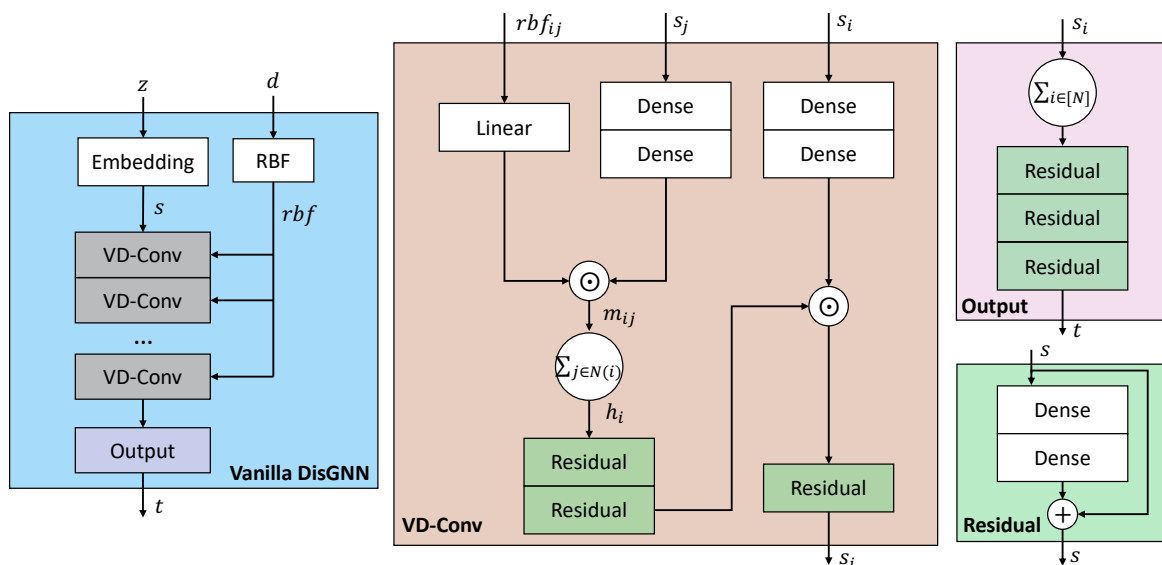


Figure 9. Architecture of Vanilla DisGNN.  $z, d, t$  represent the atomic number, euclidean distance and the target output, respectively. Each Linear block represents an affine transformation with learnable parameters  $W, b$ , while the Dense block extends the Linear block by incorporating a non-linear activation function.  $\odot$  represents Hadamard product.

We set the number of VD-Conv layers to 6. The hidden dimension is set to 512 and the dimension of radial basis functions (RBF) is set to 16. The message passing cutoff is set to 13Å for rMD17 and 7Å for MD22. We employ the polynomial envelope with  $p = 5$ , as proposed in Gasteiger et al. (2019), along with the corresponding cutoff.

**GeoNGNN.** The high-level architecture of GeoNGNN is described in Definition 4.1. The inner Vanilla DisGNN, which runs on the ego subgraph of each node, is similar to the Vanilla DisGNN block shown in Figure 9. However, the inner Vanilla DisGNN additionally performs node marking and distance encoding for each node  $j$  in node  $i$ ’s subgraph *before* passing their representations to VD-Conv layers:

$$h_{ij} \leftarrow h_j \odot \text{MLPs}(\text{RBF}(d_{ij})) \odot \text{MLPs}(\text{Emb}(\mathbb{1}_{j=i})) \quad (3)$$

where  $h_{ij}$  represents node  $j$ ’s representation in  $i$ ’s subgraph.

The outer Vanilla DisGNN additionally fuses the subgraph representation  $t_i$  produced by the inner Vanilla DisGNN for node  $i$  with  $h_i$  obtained from the embedding layer:

$$h_i \leftarrow \text{MLPs}([h_i, t_i]) \tag{4}$$

The hidden dimension and message passing cutoff are set to the same values as those in Vanilla DisGNN. The subgraph size is set to 13 Å for rMD17 and 5 Å for MD22, and the maximal subgraph size is set to 25. We set  $(N_{in}, N_{out})$  as (5, 1) for rMD17 and (3, 3) for MD22. It is worth mentioning that the total number of convolutional layers is the same as that of Vanilla DisGNN. This ensures that the receptive field of the two models is roughly the same, thereby guaranteeing a relatively fair comparison.

We optimize all models using the Adam optimizer (Kingma & Ba, 2014), incorporating exponential decay and plateau decay learning rate schedulers, as well as a linear learning rate warm-up. To mitigate the risk of overfitting, we employ early stopping based on validation loss and apply exponential moving average (EMA) with a decay rate of 0.99 to the model parameters during the validation and testing phases. The models are trained on Nvidia RTX 3090 and Nvidia A100 GPUs.

## D. GeoNGNN-C: SE(3)-complete variant of GeoNGNN

### D.1. Definition and Theoretical Analysis of GeoNGNN-C

As mentioned in Section 4.1, GeoNGNN-C is designed by simply replacing the undirected distance in GeoNGNN with directed distance. The formal definition is as follows:

**Definition D.1.** The fundamental architecture of GeoNGNN remains the same, with the exception that the inner GNN for node  $k$ 's subgraph performs the subsequent message-passing operation:

$$h_{k,i}^{(t+1)} = f_{\text{mp}}(h_{k,i}^{(t)}, \{\{h_{k,j}^{(t)}, d_{k,ij}\} \mid j \in N_k(i)\}\}),$$

where  $h_{k,i}^{(t)}$  represents node  $i$ 's representation at timestep  $t$  in node  $k$ 's subgraph, and the directed distance,  $d_{k,ij}$ , is defined as:

$$d_{k,ij} = f_{\text{dist}}(\text{sign}(\vec{r}_{ci} \times \vec{r}_{cj} \cdot \vec{r}_{ck}), d_{ij}),$$

where  $c$  is the geometric center of the geometric graph.

As can be easily validated, directed distance is invariant under SE(3)-transformation while undergoing a sign reversal after reflecting the geometric graph. Consequently, GeoNGNN-C retains SE(3)-invariance while possessing the potential to discriminate enantiomers. Significantly, we show that GeoNGNN-C is SE(3)-complete, able to distinguish all pairs of enantiomers:

**Theorem D.2.** (SE(3)-Completeness of GeoNGNN-C) When the conditions described in Theorem 4.2 are met, GeoNGNN-C is SE(3)-complete.

The formal proof is referred to Appendix F.8.

### D.2. Experimental Evaluation of GeoNGNN-C

**Datasets and tasks.** We evaluate the ability of GeoNGNN-C to distinguish enantiomers and learn meaningful chirality-relevant representations through three tasks on two datasets (Adams et al., 2021; Gaiński et al., 2023): 1) Classification of tetrahedral chiral centers as R/S. R/S offers a fundamental measure of molecular chirality, and this classification task serves as an initial evaluation of the model's capacity to discriminate enantiomers. The underlying dataset contains a total of 466K conformers of 78K enantiomers with a single tetrahedral chiral center. 2) Enantiomer ranking task and binding affinity prediction task. The two tasks share the same underlying dataset, while the second task requires models to predict the binding affinity value for each enantiomer directly, and the first requires the model to predict which enantiomer between the corresponding pair exhibits higher such values. Chirality is essential here because enantiomers often exhibit distinct behaviors when docking in a chiral protein pocket, thus leading to differences in binding affinity. The underlying dataset contains 335K conformers from 69K enantiomers carefully selected and labeled by Adams et al. (2021).

**Model architecture and training/evaluation details.** In the task of R/S classification, GeoNGNN-C adopts a three-layer outer GNN positioned *before* the inner GNNs. This configuration is designed to enhance the node features first, facilitating

Table 5. Results on chiral-sensitive tasks compared to reference models. We **bold** the best result among models and underline the second best ones.

Model	R/S	Enantiomer ranking	Binding affinity
	Accuracy $\uparrow$	R. Accuracy $\uparrow$	MAE $\downarrow$
DMPNN+tags	-	0.701 $\pm$ 0.003	0.285 $\pm$ 0.001
SphereNet	<u>0.982<math>\pm</math>0.002</u>	0.686 $\pm$ 0.003	-
Tetra-DMPNN	0.935 $\pm$ 0.001	0.690 $\pm$ 0.006	0.324 $\pm$ 0.02
ChiRo	0.968 $\pm$ 0.019	0.691 $\pm$ 0.006	0.359 $\pm$ 0.009
ChiENN	<b>0.989<math>\pm</math>0.000</b>	<b>0.760<math>\pm</math>0.002</b>	0.275 $\pm$ 0.003
GeoNGNN-C	0.980 $\pm$ 0.002	<u>0.751<math>\pm</math>0.003</u>	<b>0.254<math>\pm</math>0.000</b>

the subsequent extraction of chirality-related properties within the inner GNNs. For the other two tasks, GeoNGNN-C consists of five inner layers and one outer layer, with the outer GNN placed after the inner GNN. The model is trained with L1 loss. Specifically, if predicted affinity difference between two enantiomers falls below the threshold of 0.001, it is considered that the model lacks the capability to discriminate between the two enantiomers. Note that all the evaluation criteria are consistent with previous works (Adams et al., 2021; Gaiński et al., 2023) for fair comparisons.

**Models to compare with.** We compare GeoNGNN-C against previous high-performance models, SphereNet (Liu et al., 2021), ChiRo (Adams et al., 2021), ChiENN (Gaiński et al., 2023), and other baseline models in (Pattanaik et al., 2020; Adams et al., 2021; Gaiński et al., 2023). It is worth noting that, for the last two tasks, the docking scores are labeled at the stereoisomer level, meaning that all different conformers of a given enantiomer are assigned the same label, specifically the best score, by Adams et al. (2021). As a result, 2D Graph Neural Networks (GNNs) such as DMPNN+tags and models that possess **invariance to conformer-level transformations**, such as bond rotations, including ChiRo (Adams et al., 2021), Tetra-DMPNN (Pattanaik et al., 2020) and ChiENN (Gaiński et al., 2023), inherently exhibit significantly better data efficiency and usually exhibit better performance. GeoNGNN-C and SphereNet do not exhibit such invariance, and are trained on 5 conformers for each enantiomer as data augmentation.

**Results.** The experimental results for the three tasks are presented in Table 5. It can be observed that GeoNGNN-C demonstrates a competitive performance compared to SOTA methods on the R/S classification task. Importantly, despite the simple and general model design, GeoNGNN-C outperforms models specifically tailored for the last two tasks, such as ChiRo and ChiENN, which incorporates invariance to bond rotations. It successfully learns the *approximate invariance* from only 5 conformers per enantiomer and achieves the second-best result (very close to the best one) on the enantiomer ranking task and new SOTA results on the binding affinity prediction task. These results reveal the potential of GeoNGNN-C as a simple but theoretically chirality-aware expressive geometric model.

## E. GeoNGNN with Sampling Policies

In this appendix, we explore several efficient sampling policies for local anchors that maintain permutation invariance, without requiring the pooling of all local anchors like GeoNGNN. We evaluate the experimental performance of these sampling policies on a subset of representative molecules from the rMD17 dataset.

Surprisingly, our results demonstrate that all of the sampling strategies consistently lead to a decrease in performance. This observation may be attributed to the unfaithfulness of these alternative sampling methods in capturing the characteristics of physical/chemical systems. Consequently, these theoretical results mainly serve as **negative results**, demonstrating that the proposed GeoNGNN, described in the main body of this paper, is a much better choice, which is superior in both theoretical and experimental performance.

### E.1. Node-type Sampling

In this case, we only sample the subgraphs of local anchors  $i$  that satisfy  $X_i = X^*$ , where  $X^*$  is the specified initial node feature, and run inner GNN only on these subgraphs. For example, in molecule systems, we only sample subgraphs of all  $C$  atoms or  $H$  atoms.

In outer GNN, the initial representation of a node depends on whether it is the sampled local anchor. If the node is sampled, its initial representation is obtained by fusing its given initial feature with the subgraph representation summarized by inner

Table 6. MAE loss of node-type sampling policy on revised MD17. Energy (E) in kcal/mol, force (F) in kcal/mol/Å. C, H, N, O represents the GeoNGNN employing sampling policy with corresponding atoms. We **bold** the best result among models adopting sampling policies, and underlines the second best.

Molecule	Target	GeoNGNN	C	H	O
aspirin	E	0.0490	<b>0.0698</b>	0.0887	0.0984
	F	0.1733	<b>0.2304</b>	<u>0.3003</u>	0.3237
ethanol	E	0.0090	<u>0.0113</u>	<b>0.0104</b>	0.0164
	F	0.0616	<u>0.0758</u>	<b>0.0678</b>	0.1019
naphthalene	E	0.0083	<u>0.0129</u>	<b>0.0112</b>	-
	F	0.0437	<b>0.0451</b>	<u>0.0616</u>	-
salicylic acid	E	0.0165	<b>0.0243</b>	<u>0.0261</u>	0.0740
	F	0.0897	<b>0.1175</b>	<u>0.1379</u>	0.2779
uracil	E	0.0108	<u>0.0230</u>	<b>0.0216</b>	0.0277
	F	0.0716	<b>0.1355</b>	<u>0.1403</u>	0.1735

GNN. On the other hand, if the node is not sampled, its initial representation is calculated by only embedding its initial feature, but with different parameters.

We evaluate the sampling policy on C-type, H-type, and O-type, respectively, with the results outlined in Table E.1. There are two main phenomena. 1) Models that adopt node-type sampling policies consistently demonstrate worse performance compared to the main model, GeoNGNN, which leverages Vanilla DisGNN on all atoms. 2) A common trend can be observed: typically, the model yields better performance when more local anchors are sampled. For example, in the cases of aspirin, where there are 9, 8, and 4 atoms of C, H, O respectively, the performance matches the aforementioned pattern. Likewise, for ethanol, with 2, 6, and 1 atoms of C, H, O respectively, the pattern persists. This phenomenon may be attributed to the fact that the learning of more balanced representations of subgraphs translates to a more favorable inductive bias for prediction.

## E.2. GeoNGNN-P

Another possible sampling way, which can be more general, is to first perform graph partition based on Euclidean distance metric, splitting the graph into  $K$  clusters, where  $K$  is a hyper-parameter that can be controlled. Then, for each cluster, we can introduce a virtual node by simply calculate the cluster’s geometric center. Finally, we only sample these virtual nodes as the local anchors. We name this design as GeoNGNN-P, where  $P$  represents partitioning. The overall architecture is illustrated in Figure 10.

There are three main design principles for this:

1. **Partitioning method.** We provide two candidate partitioning methods for GeoNGNN-P. The first is METIS (Abou-Rjeili & Karypis, 2006), a widely recognized and efficient graph clustering method. We utilize the inverse of Euclidean distance as the metric, ensuring that nodes close to each other are more likely to be assigned to the same cluster. This approach effectively incorporates a geometric prior into the geometric graph. The second is BRICS (Degen et al., 2008), a chemical-specific method designed for partitioning molecules into 16 fragment prototypes (chemical motifs). While BRICS is tailored for chemical settings, it may not possess the same level of generality as METIS. Nevertheless, BRICS incorporates good chemical prior into the geometric graph, offering potential advantages in domain-specific applications.

In METIS, the value of cluster number  $K$  is adjustable, whereas in BRICS it is not. It is worth noting that when considering BRICS or METIS with a fixed finite  $K$ , there is **no assurance** that all geometric graphs can be identified, as the virtual nodes may all coincide with the geometric center. Nevertheless, METIS can effectively identify all known unidentifiable cases for Vanilla DisGNN, thereby greatly boosting expressiveness.

2. **Subgraph radius.** Theoretically, in order to achieve theoretical completeness, the subgraph radius for each local anchor should be infinite, as stated in Theorem 4.2. However, for practical reasons, we set the subgraph radii to finite numbers to enhance efficiency. Specifically, the subgraph radius  $r$  can be decomposed into two terms:  $r = r_{\text{cluster}} + r_{\text{overlap}}$ .

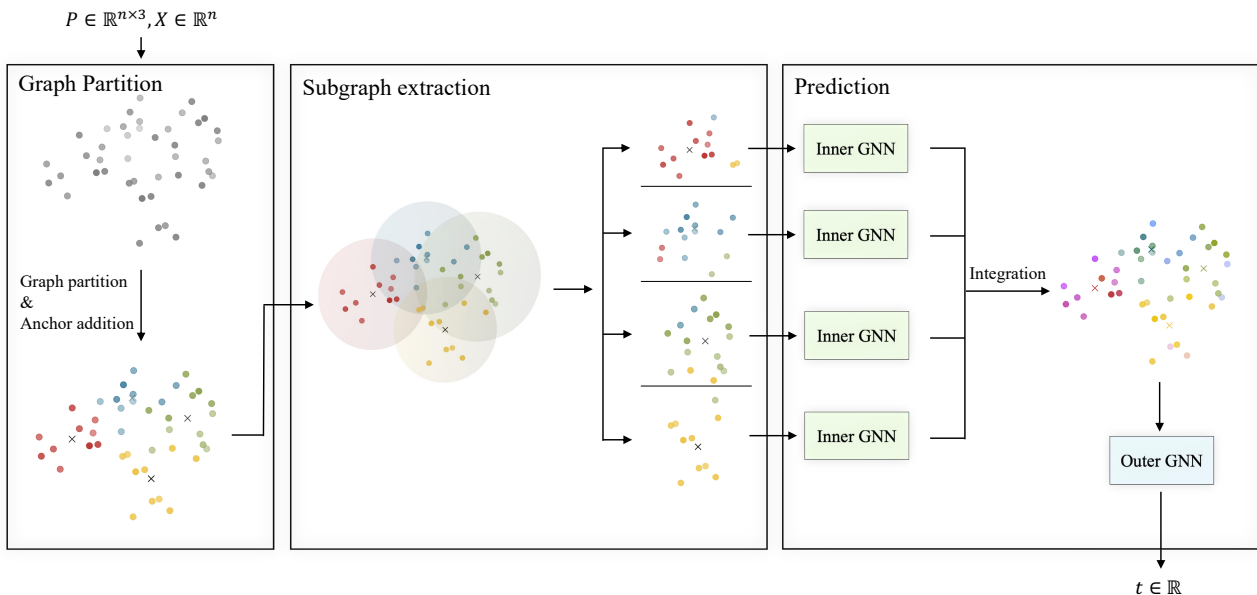


Figure 10. Overview of GeoNGNN-P. There are three main steps: Graph partition, subgraph extraction, and prediction. In Graph Partition figure, colors indicate partitions, while in Prediction figure, colors indicates initial node features for outer GNN.

Here,  $r_{\text{cluster}}$  represents the maximum distance between the cluster center and the nodes within the cluster, while  $r_{\text{overlap}}$  is a hyper-parameter that determines the extent of overlap between different cluster subgraphs.

- Initial node representations in the outer GNN.** We assign each node  $i$  its initial representation in the outer GNN as the average representation calculated within all the subgraph it belongs to, ensuring smoothness and maximum geometric information reservation.

We evaluate GeoNGNN-P with BRICS and METIS (with different  $k$  ratio) on rMD17, and the results are reported in Table E.2. 1) Similarly to the node-sampling policy, the accuracy of predictions improves as METIS produces more clusters. The performance closest to the main model, GeoNGNN, is achieved when METIS produces clusters with  $K = N \times 0.5$ . 2) Despite incorporating chemical priors, BRICS produces too few clusters (such as naphthalene and uracil, where it even cannot further split the molecule), and therefore produce bad prediction.

These findings highlight that while adopting partition methods and sampling fewer local anchors can enhance efficiency and valuable geometric/chemical prior, having too few local anchors significantly worsens performance. This observation aligns with the trends observed in node-sampling policies.

## F. Proof

### F.1. Equivalence of Reconstruction and Completeness

Given a permutation- and  $E(3)$ -invariant function  $f$ , it is apparent that  $f$  is  $E(3)$ -complete  $\iff f$  is capable of identifying all geometric graphs, simply by definition. Hence, our goal is to show that for any geometric graph  $G$ ,  $f(G) \rightarrow G$  up to permutation and  $E(3)$ -transformation  $\iff$  if  $f$  is  $E(3)$ -complete.

We now consider all  $E(3)$ -isomorphic geometric graphs as one single element in a new input space  $\mathcal{I}$ . Consequently,  $f(G) \rightarrow G$  up to permutation and  $E(3)$ -transformation is equivalent to asserting that  $f(I) \rightarrow I$ , and the definition of  $E(3)$ -completeness is:  $\forall I_1, I_2 \in \mathcal{I}, f(I_1) = f(I_2) \iff I_1 = I_2$ . Note that both statements are equivalent to that  $f$  is an injective encoder on  $\mathcal{I}$ . Thus, the two statements are equivalent to each other.

Table 7. MAE loss of GeoNGNN-P on revised MD17. Energy (E) in kcal/mol, force (F) in kcal/mol/Å. METIS ( $k$ ) represents the model adopts splitting which splits the graph into  $K = k * N$  clusters. We **bold** the best result among all GeoNGNN-P designs, and underlines the second best.

Molecule	Target	GeoNGNN	METIS (0.1)	METIS (0.3)	METIS (0.5)	BRICS
aspirin	E	0.0490	0.3476	0.4892	<u>0.3401</u>	<b>0.1508</b>
	F	0.1733	0.6734	0.5702	<b>0.4025</b>	<u>0.4833</u>
ethanol	E	0.0090	0.0160	<u>0.0157</u>	<b>0.0134</b>	0.0190
	F	0.0616	<u>0.1028</u>	0.1040	<b>0.0910</b>	0.1169
naphthalene	E	0.0083	0.1277	<u>0.1203</u>	<b>0.0129</b>	0.1411
	F	0.0437	0.4416	<u>0.3664</u>	<b>0.0682</b>	0.4567
salicylic acid	E	0.0165	0.1637	<u>0.0601</u>	<b>0.0225</b>	0.0661
	F	0.0897	0.5908	<u>0.2674</u>	<b>0.1175</b>	0.3465
uracil	E	0.0108	0.2404	<u>0.0714</u>	<b>0.0127</b>	0.1182
	F	0.0716	0.7274	<u>0.3995</u>	<b>0.0816</b>	0.5546

## F.2. Proof of Proposition A.3

1.  $|\mathbf{A}(G)| = 1 \implies$  all  $X_k^*$ -type geometric centers coincide.

This is trivially true, because the  $X_k^*$ -type geometric center is simply a specific type of global anchor. Since all global anchors coincide, it follows that all  $X_k^*$ -type geometric centers also coincide.

2. All  $X_k^*$ -type geometric centers coincide  $\implies |\mathbf{A}(G)| = 1$ .

Denote  $I_k = \{i \mid X_i = X_k^*, \forall i \in [n]\}$  as the index set. Let  $m_k^* = m(X_k^*)$  represent the mass of the  $X_k^*$  global anchor. Let  $M_k^* = \sum_{i \in I_k} m_k^*$  denote the sum of masses associated with the  $X_k^*$  global anchor. Represent the  $X_k^*$ -type geometric centers as  $A_k^* \in \mathbb{R}^3$ .

For an arbitrary global anchor  $A^m(G)$  defined by  $m$ , we have  $A^m(G) = \frac{\sum_{i \in [n]} m(X_i) P_i}{\sum_{i \in [n]} m(X_i)}$  by definition, which can be decomposed as follows:

$$\begin{aligned}
 A^m(G) &= \frac{\sum_{i \in [n]} m(X_i) P_i}{\sum_{i \in [n]} m(X_i)} \\
 &= \frac{\sum_{k \in [K]} \sum_{i \in I_k} m_k^* P_i}{\sum_{k \in [K]} \sum_{i \in I_k} m_k^*} \\
 &= \frac{\sum_{k \in [K]} A_k^* M_k^*}{\sum_{k \in [K]} M_k^*} \tag{5}
 \end{aligned}$$

Since all  $A_k^*$  coincide, denoted as  $A$ , we have:  $A^m(G) = \frac{A \sum_{k \in [K]} M_k^*}{\sum_{k \in [K]} M_k^*} = A$ . Thus, all the global anchors coincide.

## F.3. Proof of Theorem 3.4

We describe the reconstruction function  $f$  that takes Vanilla DisGNNs' output  $v$  as input and produces the geometric graph  $G$  up to permutation and E(3)-transformation. We initially assume that the point cloud *does not degenerate into 2D*, which is a trivial case and will be discussed at the end of the proof.

Initially, the output  $v$  of a 2-round Vanilla DisGNN is provided. Under the injectivity assumption of Vanilla DisGNN, it can be inferred that  $v \rightarrow \{h_i^{(2)} \mid i \in [n]\}$ . Note that  $h_i^{(2)} \rightarrow h_i^{(1)} \rightarrow h_i^{(0)} \rightarrow (d_{i,A_1}, d_{i,A_2}, d_{A_1,A_2})$ , implying that the structure of the triangle formed by  $i, A_1, A_2$  can be ascertained from  $h_i^{(2)}$ . Since nodes can receive information about the triangular shapes formed by other nodes and the two anchors during the message passing process, it is feasible to determine

the following dihedral angle list from  $h_i^{(2)}$ :

$$\begin{aligned}
 h_i^{(2)} &= \text{HASH}(h_i^{(1)}, \{(h_j^{(1)}, d_{ij}) \mid j \in [n]\}) \\
 &\rightarrow \{(h_i^{(1)}, h_j^{(1)}, d_{ij}) \mid j \in [n]\} \\
 &\rightarrow \{(h_i^{(0)}, h_j^{(0)}, d_{ij}) \mid j \in [n]\} \\
 &\rightarrow \{(d_{ij}, d_{i,A_1}, d_{i,A_2}, d_{j,A_1}, d_{j,A_2}, d_{A_1,A_2}) \mid j \in [n]\} \\
 &\rightarrow \{\theta(iA_1A_2, jA_1A_2) \mid j \in [n]\}.
 \end{aligned}$$

Here,  $\theta(iA_1A_2, jA_1A_2)$  represents the dihedral angle formed by plane  $iA_1A_2$  and plane  $jA_1A_2$ . If  $i$  or  $j$  lies on the line  $A_1A_2$ , or the angle  $\theta$  is 0, we define/overwrite  $\theta$  as  $+\infty$ .

Given this observation, we now conduct a search across the multiset  $\{h_i^{(2)} \mid i \in [n]\}$  to find the node  $x$  which can derive the smallest  $\theta(xA_1A_2, yA_1A_2)$  relative to some other node  $y$  (In case of multiple minimal angles, an arbitrary  $x$  is chosen.). Denote the minimal angle as  $\alpha$ , and we record the corresponding  $h_x^{(2)}$ . And note that since  $\theta(xA_1A_2, yA_1A_2)$  is derived from  $(h_x^{(1)}, h_y^{(1)}, d_{xy})$ , the corresponding  $(h_y^{(1)}, d_{xy})$  in the calculation of  $h_x^{(2)}$  can also be recorded. We now aim to prove that the entire geometry can be reconstructed using  $h_x^{(2)}$  and the corresponding  $(h_y^{(1)}, d_{xy})$ .

First of all, having found the node  $y$  in the multiset, we can calculate the exact 3D coordinates of nodes  $x, y, A_1, A_2$  up to  $E(3)$  transformation given  $(h_x^{(2)}, h_y^{(1)}, d_{xy})$ . This is because  $(h_x^{(2)}, h_y^{(1)}, d_{xy}) \rightarrow (d_{xy}, d_{x,A_1}, d_{x,A_2}, d_{y,A_1}, d_{y,A_2}, d_{A_1,A_2})$ . At this stage, the coordinates of  $n - 2$  nodes remain undetermined.

We proceed to traverse all nodes in the multiset  $\{(h_j^{(1)}, d_{xj}) \mid j \in [n]\}$  that can be derived from  $h_x^{(2)}$  by definition. For each node  $j$ , with information  $(h_x^{(1)}, h_j^{(1)}, d_{xj})$ , we can derive  $(d_{jx}, d_{j,A_1}, d_{j,A_2})$ . Consequently, we can determine the 3D coordinates of  $j$  to at most two positions, which are symmetrically mirroring w.r.t. the plane  $xA_1A_2$ . Notably,  $j$ 's position is unique if and only if it lies on the plane  $xA_1A_2$  (denoted as  $x$ -plane). We first identify all nodes on the  $x$ -plane, since their calculated positions are unique.

Additionally, from  $h_y^{(1)}$ , we can also derive  $(d_{jy}, d_{j,A_1}, d_{j,A_2})$  for each node  $j$ , allowing us to identify all nodes on the  $y$ -plane.

The coordinates of these nodes are added to the ‘‘known’’ set of nodes  $K$ , while the remaining nodes are labeled as ‘‘unknown.’’

It is established that there are no ‘‘unknown’’ nodes in the interior (as  $\theta_{xA_1A_2, yA_1A_2}$  is minimal) and border (since we have identified these points) of the  $x$ -plane and  $y$ -plane. We denote the interior and border of the two planes as  $P_0$ .

Now, we reflect the  $y$ -plane mirrorly w.r.t. the  $x$ -plane which yields the  $p_{-1}$ -plane. The interior and border formed by  $p_{-1}$ -plane and  $x$ -plane are denoted as  $P_{-1}$ . Since there are no ‘‘unknown’’ nodes in  $P_0$ , the remaining undetermined nodes in  $P_{-1}$  can be determined from  $h_x^{(2)}$ , as their another possible position calculated by  $h_x^{(2)}$  lie in the ‘‘dead area’’  $P_0$ , where it is ensured to be empty (no undetermined nodes left). Similarly, reflecting the  $x$ -plane w.r.t. the  $y$ -plane produces the  $p_1$ -plane, and the corresponding area by  $p_1$ -plane and  $y$ -plane is denoted as  $P_1$ . Nodes in  $P_1$  are determined likewise from  $h_y^{(1)}$ . This process continues by reflecting the  $p_1$ -plane w.r.t. the  $x$ -plane to obtain the  $p_{-2}$ -plane, determining the nodes in  $P_{-2}$ , and so forth, until all  $P$  areas collectively cover the entire 3D space. Consequently, all nodes can be determined, and the geometric structure can be reconstructed.

When the geometric graph degenerates into 2D, we can initially derive a node  $i$ 's representation  $h_i^{(2)}$  from the output  $v$  of Vanilla DisGNN that does not lie on the line  $A_1A_2$ . By leveraging  $h_i^{(2)}$ , we can extract the necessary distance information to compute the coordinates of  $i, A_1$ , and  $A_2$  up to  $E(3)$ -transformation. Given that  $h_i^{(2)} \rightarrow \{(h_j^{(1)}, d_{ij}) \mid j \in [n]\}$ , we can derive  $(d_{ij}, d_{jA_1}, d_{jA_2})$  from each  $(h_j^{(1)}, d_{ij})$ . Consequently, the coordinates of node  $j$  can be uniquely determined (2D setting). And therefore, the complete geometry can be reconstructed up to  $E(3)$ -transformation.

#### E.4. Proof of Proposition 3.2 and Proposition A.1

Like the previous subsection, we describe the algorithm  $f$  that takes the left-end representations of ‘‘derive’’ as input and outputs the right-end representations. We first give the proof of Proposition 3.2, and at the end, we additionally explain the

proof of Proposition A.1.

**Node-GA distance.**

Denote  $f(m, i) = \sum_{j \in [n]} m(X_j) d_{ij}^2$ . It is noteworthy that  $f(m, i)$  can be derived from  $h_i^{(1)}$ , since  $h_i^{(1)} \rightarrow (h_i^{(0)}, \{(h_j^{(0)}, d_{ij}) \mid j \in [n]\}) \rightarrow \{(X_j, d_{ij}) \mid j \in [n]\}$  (note that  $m$  is given).

$f(m, i)$  can be decomposed as:

$$\begin{aligned}
 f(m, i) &= \sum_{j \in [n]} m(X_j) d_{ij}^2 \\
 &= \sum_{j \in [n]} m(X_j) \|P_i - P_j\|^2 \\
 &= \sum_{j \in [n]} m(X_j) \|P_i - A^m + A^m - P_j\|^2 \\
 &= \sum_{j \in [n]} m(X_j) (\|P_i - A^m\|^2 + \|P_j - A^m\|^2 - 2\langle P_i - A^m, P_j - A^m \rangle) \\
 &= M \|P_i - A^m\|^2 + \sum_{j \in [n]} m(X_j) \|P_j - A^m\|^2 - 2\langle P_i - A^m, \sum_{j \in [n]} m(X_j) (P_j - A^m) \rangle
 \end{aligned}$$

where  $M = \sum_{j \in [n]} m(X_j)$  and  $\langle \cdot \rangle$  denotes the inner product. By definition,  $\sum_{j \in [n]} m(X_j) (P_j - A^m) = 0$ . Thus, we have:

$$f(m, i) = M \|P_i - A^m\|^2 + \sum_{j \in [n]} m(X_j) \|P_j - A^m\|^2$$

The distance from  $i$  to  $A^m$  can be calculated as:

$$\frac{1}{M} \left( f(m, i) - \frac{1}{2M} \sum_{j \in [n]} m(X_j) f(m, j) \right) = \|P_i - A^m\|^2 = d_{i, A^m}^2 \quad (6)$$

And since

$$\begin{aligned}
 h_i^{(2)} &\rightarrow (h_i^{(1)}, \{(h_j^{(1)}, d_{ij}) \mid j \in [n]\}) \\
 &\rightarrow (f(m, i), \{(m(X_j), f(m, j)) \mid j \in [n]\}),
 \end{aligned} \quad (7)$$

we have:  $h_i^{(2)} \rightarrow d_{i, A^m}$ .

**GA-GA distance.**

According to Node-GA distance, at round 2, each node is aware of its distance to the two anchors:

$$h_i^{(2)} \rightarrow (d_{i, A^{m_1}}, d_{i, A^{m_2}}) \quad (8)$$

Then, we have:

$$\begin{aligned}
 h_i^{(2)} &\rightarrow \|P_i - A^{m_1}\|^2 - \|P_i - A^{m_2}\|^2 \\
 &= \langle A^{m_2} - A^{m_1}, 2P_i - A^{m_1} - A^{m_2} \rangle
 \end{aligned}$$

The following derivation holds:

$$\begin{aligned}
 \{\{h_i^{(2)} \mid i \in [n]\}\} &\rightarrow \{\{h_i^{(2)}, m_1(X_i) \mid i \in [n]\}\} \\
 &\rightarrow \frac{1}{M_1} \sum_{i \in [n]} m_1(X_i) \langle -A^{m_1} + A^{m_2}, 2P_i - A^{m_1} - A^{m_2} \rangle \\
 &= \langle -A^{m_1} + A^{m_2}, (\frac{2}{M_1} \sum_{i \in [n]} m_1(X_i) P_i) - A^{m_1} - A^{m_2} \rangle \\
 &= \langle -A^{m_1} + A^{m_2}, 2A^{m_1} - A^{m_1} - A^{m_2} \rangle \\
 &= \langle -A^{m_1} + A^{m_2}, A^{m_1} - A^{m_2} \rangle \\
 &= -\|A^{m_1} - A^{m_2}\|^2
 \end{aligned} \tag{9}$$

where  $M_1 = \sum_{i \in [n]} m_1(X_i)$ . This provides the distance between the two anchors.

### Counting Global Anchors.

According to previous proof,  $v_G$  can derive the set  $AD = \{d_{A^{X^*}, A^c} \mid X^* \in \{X_i \mid i \in [n]\}\}$ . Here,  $A^{X^*}$  represents the  $X^*$ -type center of  $G$ , while  $A^c$  represents the geometric center.

According to Proposition A.3, global anchor set degenerates into one point  $\iff$  all  $A^{X^*}$  coincide. Therefore, we can determine whether the global anchor set degenerates based on  $AD$ .

If  $AD = \{0\}$ , we can conclude that all the  $X^*$ -type center coincide with the geometric center; therefore, global anchor degenerates, i.e.,  $|\mathbf{A}(G)| = 1$ .

And if  $AD$  contains non-zero elements, then at least one  $X^*$ -type center is different from the geometric center. Note that  $A^{X^*}$  and  $A^c$  are all in  $\mathbf{A}(G)$ ; therefore,  $|\mathbf{A}(G)| > 1$ .

As such, the sequence proceeds as follows:  $v_G \rightarrow AD \rightarrow \mathbb{1}_{AD \text{ contains non-zero elements}} \rightarrow \mathbb{1}_{|\mathbf{A}(G)|=1}$ .

### Proof of Proposition A.1

Based on previous proof, it has been shown that starting from the node representation  $h_i^{(2)}$  generated by a two-round Vanilla DisGNN, we have that  $h_i^{(2)} \rightarrow d_{i, A^c}$ . This indicates that a two-round Vanilla DisGNN is capable of performing Center Enhancement ( $\mathcal{C}$ ). Furthermore, since the node individualization performed by an infinite-round Vanilla DisGNN is no coarser than that of the two-round Vanilla DisGNN, we can conclude that  $\mathbf{A}^{\mathcal{C}}(G) \subseteq \mathbf{A}^{\mathcal{VD}}(G)$ .

The iterations of Vanilla DisGNN can be manually divided into two distinct phases. In the first phase, the algorithm continues to run until there is no further change in the node individualization. This phase focuses on enhancing the node features and expanding the global anchors to  $\mathcal{VD}$  enhanced global anchors. In the second phase, Vanilla DisGNN operates on the augmented geometric graph for two additional rounds. Analogous to the previous proof, we can derive all the distance encoding information pertaining to  $\text{GA}^{\mathcal{VD}}$ .

### F.5. Proof of Theorem 3.5 and Theorem A.2

Here, we first prove Theorem 3.5, and at the end explains the proof of Theorem A.2.

We prove the equivalent converse condition: Given a geometric graph  $G$ , if  $|\mathbf{A}(G)| > 1$ , then for any graph  $G'$  that is not E(3)-isomorphic to  $G$ , Vanilla DisGNN will produce different outputs for them.

Let  $A_1$  and  $A_2$  be two arbitrary distinct anchors in  $\mathbf{A}(G)$ . According to Proposition 3.2, Vanilla DisGNN can automatically learn the distance information among node  $i$ ,  $A_1$  and  $A_2$ , enabling it to perform APE w.r.t. the two anchors. Then, based on Theorem 3.4, one can reconstruct  $G$  up to permutation and E(3) transformation from the encoding vector  $v_G \in \mathbb{R}^k$  produced by Vanilla DisGNN for  $G$ .

Now, consider an arbitrary geometric graph  $G'$  that is not E(3)-isomorphic to  $G$ .

If  $|\mathbf{A}^{\mathcal{VD}}(G')| > 1$ , we can reconstruct  $G'$  up to permutation and E(3)-transformation from the encoding vector  $v_{G'}$  produced by Vanilla DisGNN. By comparing these two reconstructed geometric graphs, we can conclude  $v_{G'} \neq v_G$ .

If  $|\mathbf{A}^{\mathcal{V}^D}(G')| = 1$ , based on the ‘‘Counting GA’’ item in Proposition 3.2, we can also prove that  $v_{G'} \neq v_G$ , since  $v_{G'} \rightarrow False$  (No more than 1 global anchor) while  $v_G \rightarrow True$  (Multiple global anchor).

We can similarly prove Theorem 3.5 by leveraging Proposition A.1 instead of Proposition 3.2.

## E.6. Proof of Theorem 4.2

Based on the condition that  $r_{\text{sub}} = \infty$ , all the subgraphs contain all the nodes in the entire graph.

Considering a subgraph of some node  $i$ , and let’s first assume that node  $i$  is distinct to the geometric center  $c$ . Here, for simplicity, we denote node  $j$ ’s representation in subgraph  $i$  using  $h_j$  instead of  $h_{ij}$  since the context is clear.

1. After 1 round of Vanilla DisGNN, for all  $j \in [n]$ ,  $h_j^{(1)}$  can derive  $d_{ij}$ .
2. After 2 rounds of Vanilla DisGNN, according to Proposition 3.2, for all  $j \in [n]$ ,  $h_j^{(2)}$  can derive  $d_{jc}$ .
3. After 3 rounds of Vanilla DisGNN, for all  $j \in [n]$ ,  $h_j^{(3)}$  can derive  $d_{ic}$ .

At this point, for all nodes  $j$ ,  $h_j^{(3)}$  can derive  $d_{ji}$ ,  $d_{jc}$ , and  $d_{ic}$ , thus completing the APE related to  $i$  and  $c$ . Then:

4. At round 5, according to Theorem 3.4, the output of Vanilla DisGNN w.r.t. the subgraph of node  $i$ ,  $s_i = f_{\text{output}}(\{\{h_j^{(5)} \mid j \in [n]\}\})$ , can derive the unique E(3)- and permutation-invariant identifier of the geometric graph.

Note that there is still a problem with the above proof: node  $i$  may coincide with the geometric center, which does not satisfy the assumption that two anchors are distinct in Theorem 3.4. For instance, consider a point cloud that forms a sphere and has a spherical center. If we choose the spherical center as node  $i$ , then there is only one anchor, which is node  $i$  itself. However, since GeoNGNN pools all the subgraph representations  $s_i$  injectively in the outer GNN and obtains the final output  $s$ , there must exist one node that does not coincide with any global anchor. And since the outer GNN is injective,  $s$  can always derive the E(3)- and permutation-invariant identifier of the geometric graph.

## E.7. Proof of Theorem 4.3

### E.7.1. DIMENET’S E(3)-COMPLETENESS

To begin, let us abstract the functions utilized in DimeNet. Fundamentally, DimeNet employs edge representations, iteratively updating these representations based on the neighbors of edges within a specified neighbor cutoff. During aggregation, DimeNet incorporates angle information formed by the center edge and its neighbor edges. Finally, all these edge representations are aggregated to produce a graph-level output.

Let us formally state these procedures.

**Initialization (DimeNet).** In DimeNet, the initial representation  $h_{ij}$  of the edge  $ij$  is initialized based on the tuple  $(z_i, z_j, d_{ij})$ , where  $z_i$  and  $z_j$  are the features of nodes  $i$  and  $j$ , and  $d_{ij}$  is the distance between these nodes:

$$h_{ij} = f_{\text{init}}^{\text{DimeNet}}(z_i, z_j, d_{ij}) \quad (10)$$

**Message Passing (DimeNet).** The message passing in DimeNet updates the edge representation  $h_{ij}$  based on the features of neighboring edges and their respective geometric information. It aggregates information from all neighbors  $k$  of node  $i$ :

$$h_{ij} = f_{\text{update}}^{\text{DimeNet}}(h_{ij}, \{\{(\theta_{kij}, h_{ki}, d_{ij}) \mid k \in N(i)\}\})$$

Note that  $h_{ij}$  is initialized by fusing  $d_{ij}$  and atomic information, therefore we have:  $h_{ij} \rightarrow d_{ij}$ . And clearly  $d_{ij}, d_{ik}, d_{kj} \rightarrow \theta_{kij}$ . Therefore, the above function is expressively equivalent to:

$$h_{ij} = f_{\text{update}}^{\text{DimeNet}}(h_{ij}, \{\{d_{kj}, h_{ki} \mid k \in N(i)\}\})$$

When the message passing cutoff of DimeNet is infinite,  $N(i) = [n]$ , giving the final update function:

$$h_{ij} = f_{\text{update}}^{\text{DimeNet}}(h_{ij}, \{\{ (h_{ki}, d_{kj}) \mid k \in [n] \}\}) \quad (11)$$

**Output Pooling (DimeNet).** Finally, DimeNet pools over all node pairs to obtain the final representation  $t$ :

$$t = f_{\text{output}}^{\text{DimeNet}}(\{\{ \{ h_{ij} \mid i \in [n] \} \mid j \in [n] \}\}) \quad (12)$$

GeoNGNN, as a subtype of subgraph GNN, initializes and updates the node  $j$ 's representation in node  $i$ 's subgraph based on its atomic number and its distance to node  $i$ . Representing the node  $j$ 's representation in node  $i$ 's subgraph as  $h_{ij}$ , then we can samely abstract its function forms.

**Initialization (GeoNGNN).** GeoNGNN initializes  $h_{ij}$  based on node  $j$ 's initial node feature and distance encoding w.r.t.  $i$ :

$$h_{ij} = f_{\text{init}}^{\text{GeoNGNN}}(z_j, d_{ij}) \quad (13)$$

**Message Passing (GeoNGNN).** GeoNGNN's inner GNN iteratively updates  $h_{ij}$  based on the following procedure:

$$h_{ij} = f_{\text{update}}^{\text{GeoNGNN}}(h_{ij}, \{\{ (h_{ik}, d_{kj}) \mid k \in [n] \}\}) \quad (14)$$

Note that  $k$  iterates all nodes, because according to Theorem 4.2, the complete version GeoNGNN has infinite subgraph size and message passing cutoff.

**Output Pooling (GeoNGNN).** In the absence of an outer GNN, GeoNGNN produces the scalar output by respectively aggregating all in-subgraph nodes' representations as the subgraph representation, and then aggregating all subgraphs' representations:

$$t = f_{\text{output}}^{\text{GeoNGNN}}(\{\{ \{ h_{ij} \mid j \in [n] \} \mid i \in [n] \}\}) \quad (15)$$

**Implementing GeoNGNN with DimeNet.** Now we show how to use DimeNet to implement GeoNGNN. Since GeoNGNN is E(3)-complete, it can be observed that if DimeNet can successfully implement GeoNGNN, then DimeNet is also E(3)-complete.

Let us start by examining the initialization step. Note that  $f_{\text{init}}^{\text{DimeNet}}$  (Eq. 10) takes more information than  $f_{\text{init}}^{\text{GeoNGNN}}$  (Eq. 13) as input. Therefore, by learning a function  $f_{\text{init}}^{\text{DimeNet}}$  that simply disregards the  $z_i$  term,  $f_{\text{init}}^{\text{DimeNet}}$  can achieve the same function form as  $f_{\text{init}}^{\text{GeoNGNN}}$ .

Next, we move on to the update (message passing) step. The only difference between  $f_{\text{update}}^{\text{DimeNet}}$  (Eq. 11) and  $f_{\text{update}}^{\text{GeoNGNN}}$  (Eq. 14) lies in their input arrangements. Specifically,  $f_{\text{update}}^{\text{DimeNet}}$  takes  $h_{ki}, k \in [n]$  as part of input, while  $f_{\text{update}}^{\text{GeoNGNN}}$  takes  $h_{ik}, k \in [n]$  as the corresponding part of input. This index swap can be mathematically aligned: We can stack two DimeNet update layers to implement one GeoNGNN update layer. The first DimeNet layer, starting from  $h_{ij}^{(t)}$ , calculates  $h_{ij}^{(t+\frac{1}{2})}$  to store the information of  $h_{ji}^{(t)}$ , i.e.,  $h_{ij}^{(t+\frac{1}{2})} \rightarrow h_{ji}^{(t)}$ . This is feasible due to the property that in Eq.11,  $(d_{jj}, h_{ji})$  can be selected uniquely from the multiset by  $f_{\text{update}}^{\text{DimeNet}}$ , as  $d_{kj} = 0$  if and only if  $k = j$ . Subsequently, the second DimeNet layer swaps the indices within the multiset, transforming  $(h_{ij}^{(t+\frac{1}{2})}, \{\{ (d_{kj}, h_{ki}^{(t+\frac{1}{2})}) \mid k \in [n] \}\})$  into  $(h_{ij}^{(t)}, \{\{ (d_{kj}, h_{ki}^{(t)}) \mid k \in [n] \}\})$ . At this stage, the function form aligns with that of  $f_{\text{update}}^{\text{GeoNGNN}}$  (Eq.14).

Finally, we consider the output step. Similarly, the only distinction between  $f_{\text{output}}^{\text{DimeNet}}$  (Eq.12) and  $f_{\text{output}}^{\text{GeoNGNN}}$  (Eq.15) lies in the swapping of input indices. By stacking one DimeNet update layer and one DimeNet output layer, we can similarly implement the GeoNGNN output layer, as discussed in the prior paragraph.

In conclusion, we have shown that DimeNet's layers can be utilized to implement GeoNGNN's layers. By doing so, we establish that DimeNet is also E(3)-complete with a constant number of layers.

### F.7.2. E(3)-COMPLETENESS OF SPHERENET

We aim to demonstrate the E(3)-completeness of SphereNet by illustrating that SphereNet can implement DimeNet, which has already been established as E(3)-complete in the preceding subsection. We begin by abstracting the layers of SphereNet.

**Initialization (SphereNet).** Similar to DimeNet, SphereNet also initializes edge representations by integrating atom properties and distance information:

$$h_{ij} = f_{\text{init}}^{\text{SphereNet}}(z_i, z_j, d_{ij}) \quad (16)$$

**Message Passing (SphereNet).** During message passing, SphereNet aggregates neighbor edge information into the center edge, while additionally considering end nodes' embeddings and spherical coordinates. Since we consider SphereNet\*, which drops the relative azimuthal angle  $\varphi_k$  of end node  $k$ , the function form is highly similar to that of DimeNet:

$$h_{ij} = f_{\text{update}}^{\text{SphereNet}}(h_{ij}, v_i, v_j, \{(h_{ki}, d_{ki}, \theta_{kij}) \mid k \in [n]\})$$

Note that the original SphereNet can only be more powerful than SphereNet\*.

Since  $h_{ij} \rightarrow d_{ij}, (d_{ij}, d_{ki}, \theta_{kij}) \rightarrow d_{kj}$ , the above function is equivalently expressive as

$$h_{ij} = f_{\text{update}}^{\text{SphereNet}}(h_{ij}, v_i, v_j, \{(h_{ki}, d_{kj}) \mid k \in [n]\}) \quad (17)$$

**Output (SphereNet).** The output block of SphereNet first aggregates edge representations into node representations as follows:

$$v_j = f_{\text{node}}^{\text{SphereNet}}(\{h_{ij} \mid i \in [n]\})$$

Then, in order to calculate graph/global embedding, it further aggregates node representations as follows:

$$t = f_{\text{graph}}^{\text{SphereNet}}(\{v_j \mid j \in [n]\})$$

Therefore, the overall output function can be abstracted as:

$$t = f_{\text{output}}^{\text{SphereNet}}(\{\{h_{ij} \mid i \in [n]\} \mid j \in [n]\}) \quad (18)$$

**Implementing DimeNet with SphereNet.** Now we show how to use SphereNet to implement DimeNet.

At the initialization step,  $f_{\text{init}}^{\text{SphereNet}}$  (Eq. 16) and  $f_{\text{init}}^{\text{DimeNet}}$  (Eq. 10) exhibit exactly the same function form.

At the update step,  $f_{\text{update}}^{\text{SphereNet}}$  (Eq. 17) takes strictly more information, i.e., the node representations, than  $f_{\text{update}}^{\text{DimeNet}}$  (Eq. 11). Therefore, by learning a function  $f_{\text{update}}^{\text{SphereNet}}$  that simply ignores node representations  $v_i, v_j$ ,  $f_{\text{update}}^{\text{SphereNet}}$  and  $f_{\text{update}}^{\text{DimeNet}}$  can share the same function form.

At the output step,  $f_{\text{output}}^{\text{SphereNet}}$  (Eq. 18) and  $f_{\text{output}}^{\text{DimeNet}}$  (Eq. 12) share exactly the same function form.

In conclusion, we have shown that SphereNet's layers can be utilized to implement DimeNet's layers. By doing so, we establish that SphereNet is also E(3)-complete with a constant number of layers.

### F.7.3. E(3)-COMPLETENESS OF GEMNET

GemNet(-Q) and DimeNet share the same initialization and output block. The difference between them lies in the update block. Specifically, GemNet adopts a three-hop message passing to incorporate higher-order geometric information, dihedral angle. The update function can be abstracted as:

$$h_{ij} = f_{\text{update}}^{\text{GemNet}}(h_{ij}, \{(h_{ab}, d_{ij}, d_{bj}, d_{ab}, \theta_{ijb}, \theta_{jba}, \theta_{ijba}) \mid b \in [n], a \in [n]\})$$

Here,  $\theta_{ijba}$  that has 4 subscripts represents the dihedral angle of plane  $ijb$  and  $jba$ . By learning a function that simply selects all  $b = i$  from the multiset and ignores some terms (Note that this is feasible, since  $(h_{ab}, d_{ij}, \theta_{ijb}, \theta_{ijba}, d_{bj}, \theta_{jba}, d_{ab}) \rightarrow (d_{ij}, \theta_{ijb}, d_{bj}) \rightarrow d_{bi}$ , while only  $b = i$  results in  $d_{bi} = 0$ ),  $f_{\text{update}}^{\text{GemNet}}$  can be simplified as follows:

$$h_{ij} = f_{\text{update}}^{\text{GemNet}}(h_{ij}, \{(\theta_{aij}, h_{ai}, d_{ij}) \mid a \in [n]\}) \quad (19)$$

Now, the simplified  $f_{\text{update}}^{\text{GemNet}}$  has the same form as  $f_{\text{update}}^{\text{DimeNet}}$  (Eq. 11), indicating that GemNet can implement DimeNet, and therefore is also E(3)-complete.

### E.8. Proof of Theorem D.2

We first note that the proof is highly similar to that in the proof of Theorem 4.2.

Let us consider a subgraph containing a node  $i$ , where we assume that  $i$  is distinct from the geometric center  $c$ . By imitating the proof of Theorem 4.2, we can ascertain the following:

After three rounds of the Chiral Vanilla DisGNN (i.e., the Vanilla DisGNN that incorporates the directed distance as a geometric representation as described in Definition D.1), node representations  $h_j^{(3)}$  for any node  $j$  can encode the directed distances  $d_{ji}$ ,  $d_{jc}$ , and  $d_{ic}$ . This enables the completion of the APE related to nodes  $i$  and  $c$ .

Next, we employ a modified version of the proof from Theorem 3.4 to demonstrate that with an additional two rounds of the Chiral Vanilla DisGNN, we can derive the  $SE(3)$ - and permutation-invariant identifier of the geometric graph  $G$ .

In the proof of Theorem 3.4, we first search across all the nodes to find two nodes  $a$  and  $b$  that forms the minimal dihedral angles  $\theta(aic, bic)$ , and then identifies the coordinates of  $a, b, i, c$  up to  $E(3)$ -transformation from the all-pair distances  $D = \{(m, n, d_{mn}) \mid m, n \in \{a, b, i, c\}\}$ . However, since Chiral Vanilla DisGNN embeds the geometry using directed distance, we now have  $D_i = \{(m, n, d_{i,mn}) \mid m, n \in \{a, b, i, c\}\}$  instead. We are now able to identify the coordinates of  $a, b, i, c$  up to  $SE(3)$ -transformation from  $D_i$  in the following way:

1. Fix  $x_i = (0, 0, 0)$ .
2. Fix  $x_c = (d_{ic}, 0, 0)$ .
3. Fix  $x_a$  in plane  $xOy+$  and calculate its coordinates using  $d_{ia}, d_{ca}$ .
4. Calculate the coordinates of  $x_b$  using  $d_{ib}, d_{cb}, d_{ab}$ , and determine whether  $b$  is on  $z+$  side or  $z-$  side using the signal embedded in  $d_{i,ab}$ .

Note that the orientation relevant to  $SE(3)$  transformation is already determined at this stage. We proceed with the remaining steps of the proof outlined in Theorem 3.4 and reconstruct the whole geometry in a *deterministic* way based on the known 4-tuple  $abci$ , and therefore reconstruct the whole geometry up to permutation and  $SE(3)$ -transformation.

Similarly, note that such subgraphs  $i$ , where  $i$  is distinct from the geometric center  $c$ , always exist as GeoNGNN-C traverses all node subgraphs. Hence, we have established the  $SE(3)$ -Completeness of GeoNGNN-C.